The Astrophysical Journal, 725:1805–1823, 2010 December 20 doi:10.1088/0004-637X/725/2/1805

THE X-RAY SPECTRA OF THE LUMINOUS LMXBs IN NGC 3379: FIELD AND GLOBULAR CLUSTER SOURCES

N. J. Brassington[1], G. Fabbiano[1], S. Blake[2,3], A. Zezas[1,4,5], L. Angelini[6], R. L. Davies[3], J. Gallagher[7], V. Kalogera[8], D.-W. Kim[1], A. R. King[9], A. Kundu[10], G. Trinchieri[11], and S. Zepf[10]
[1] Harvard-Smithsonian Center for Astrophysics, 60 Garden Street, Cambridge, MA 02138, USA; nbrassington@head.cfa.harvard.edu
[2] School of Physics and Astronomy, University of Southampton, Highfield, Southampton, SO17 1BJ, UK
[3] Sub-Department of Astrophysics, University of Oxford, Oxford, OX1 3RH, UK
[4] Physics Department, University of Crete, P.O. Box 2208, 710 03 Heraklion, Crete, Greece
[5] IESL, Foundation for Research and Technology, 71110 Heraklion, Crete, Greece
[6] Laboratory for X-Ray Astrophysics, NASA Goddard Space Flight Center, Greenbelt, MD 20771, USA
[7] Department of Astronomy, University of Wisconsin, Madison, WI 53706-1582, USA
[8] Department of Physics and Astronomy, Northwestern University, Evanston, IL 60208, USA
[9] Theoretical Astrophysics Group, University of Leicester, Leicester LE1 7RH, UK
[10] Department of Physics and Astronomy, Michigan State University, East Lansing, MI 48824-2320, USA
[11] INAF-Osservatorio Astronomico di Brera, Via Brera 28, 20121 Milan, Italy
Received 2010 February 2; accepted 2010 October 10; published 2010 December 2

ABSTRACT

From a deep multi-epoch *Chandra* observation of the elliptical galaxy NGC 3379 we report the spectral properties of eight luminous LMXBs ($L_X > 1.2 \times 10^{38}$ erg s^{-1}). We also present a set of spectral simulations, produced to aid the interpretation of low-count single-component spectral modeling. These simulations demonstrate that it is possible to infer the spectral states of X-ray binaries from these simple models and thereby constrain the properties of the source. Of the eight LMXBs studied, three reside within globular clusters (GCs) and one is a confirmed field source. Due to the nature of the luminosity cut, all sources are either neutron star (NS) binaries emitting at or above the Eddington luminosity or black hole (BH) binaries. The spectra from these sources are well described by single-component models, with parameters consistent with Galactic LMXB observations, where hard-state sources have a range in photon index of 1.5–1.9 and thermally dominant (TD) sources have inner-disk temperatures between ∼0.7 and 1.55 keV. The large variability observed in the brightest GC source ($L_X > 4 \times 10^{38}$ erg s^{-1}) suggests the presence of a BH binary. At its most luminous this source is observed in a TD state with $kT_{in} = 1.5$ keV, consistent with a BH mass of $\sim 4\,M_\odot$. This observation provides further evidence that GCs are able to retain such massive binaries. We also observed a source transitioning from a bright state ($L_X \sim 1 \times 10^{39}$ erg s^{-1}), with prominent thermal and non-thermal components, to a less luminous hard state ($L_X = 3.8 \times 10^{38}$ erg s^{-1}, $\Gamma = 1.85$). In its high flux emission, this source exhibits a cool-disk component of ∼0.14 keV, similar to spectra observed in some ultraluminous X-ray sources (ULXs). Such a similarity indicates a possible link between "normal" stellar-mass BHs in a high accretion state and ULXs.

Key words: galaxies: individual (NGC 3379) – X-rays: binaries – X-rays: galaxies

Online-only material: color figures

1. INTRODUCTION

The discovery with *Chandra* of several low-mass X-ray binary (LMXB) populations in early-type galaxies and the associations of these LMXBs with either globular clusters (GCs) or the stellar field have provided new impetus to the study of the formation and evolution of LMXBs in GCs and to the possible relation of field LMXBs to the GC population (Grindlay & Hertz 1985; Verbunt & van den Heuvel 1995; see Fabbiano 2006 and references therein). Given the characteristics of these data, most of this work has been based on population studies (e.g., Kim et al. 2006; Kundu et al. 2007; Sivakoff et al. 2007; Voss & Gilfanov 2007). However, in the few cases of detection of luminous sources in deep enough observations, detailed spectral and variability studies can be pursued, to provide more direct constraints on the nature of the X-ray sources. One such example is the recent discovery of a variable luminous GC source in NGC 4472, with temporal and spectral characteristics supporting a stellar black hole (BH) binary (Maccarone et al. 2007; Shih et al. 2008).

In this paper, we report the results of the spectral analysis of eight luminous sources ($L_X > 1.2 \times 10^{38}$ erg s^{-1} in the 0.3–8.0 keV band), detected in the nearby elliptical galaxy NGC 3379 (in the poor group Leo, $D = 10.6$ Mpc; Tonry et al. 2001[12]) with *Chandra* ACIS-S (Weisskopf et al. 2000). These sources were observed at five different epochs, as part of a monitoring campaign with *Chandra* (PI: Fabbiano) providing the rare opportunity of long-term spectral monitoring of LMXBs in an elliptical galaxy. These sources are part of the sample of 132 sources detected in NGC 3379 from these observations with luminosities greater than a few 10^{36} erg s^{-1} (Brassington et al. 2008—hereafter B08).

In Section 2, we describe the observations and the properties of the sources under study from the B08 catalog. In Section 3, we describe our spectral analysis and report the results. In Section 4, we present spectral simulations that we have performed to aid

[12] Note that Jensen et al. (2003) report a distance of 9.82 Mpc. However, the distance of Tonry et al. (2001) is adopted here for consistency with Brassington et al. (2008). This choice does not affect our conclusions in any way.

Table 1
Observation Log and Source Counts

	Obs 1	Obs 2	Obs 3	Obs 4	Obs 5	All	Opt. Corr.
ObsID	1587	7073	7074	7075	7076	-	
Exposure (ks)	29.0	80.3	66.7	79.6	68.7	324.2	
Net counts							
S41	7.5 ± 10.0	146.0 ± 13.5	143.6 ± 13.2	150.0 ± 13.6	200.0 ± 15.4	718.7 ± 28.4	GC
S42	170.4 ± 14.1	457.8 ± 22.5	269.0 ± 17.6	512.8 ± 23.8	331.5 ± 19.4	1741.8 ± 43.0	GC
S67	95.4 ± 11.1	239.5 ± 16.9	219.0 ± 16.1	243.2 ± 16.9	198.7 ± 20.9	1008.9 ± 33.4	GC
S74	55.8 ± 9.0	181.1 ± 14.8	147.5 ± 13.7	158.2 ± 14.0	580.7 ± 25.5	1165.4 ± 35.9	-
S77	25.5 ± 6.7	111.1 ± 12.2	90.0 ± 11.2	92.0 ± 11.3	71.7 ± 10.1	414.4 ± 22.5	-
S86	195.7 ± 15.2	572.9 ± 25.3	371.4 ± 20.6	620.4 ± 26.2	352.4 ± 20.2	2114.3 ± 47.7	F
S102	165.5 ± 14.0	459.4 ± 22.6	332.5 ± 19.5	288.3 ± 18.2	140.2 ± 13.2	1389.0 ± 38.7	-
S103	75.1 ± 10.6	131.3 ± 12.6	127.1 ± 13.4	170.7 ± 15.1	143.1 ± 14.1	636.9 ± 26.6	-

Notes. Optical correlations: GC indicates an association with a globular cluster, F indicates a field source, which is within the *HST* FOV and has no optical association. - indicates that there is insufficient optical coverage for this source to determine an optical association. All of these classifications are fully described in B08, Section 2.6.

in the interpretation of our results, and in Section 5 we discuss the spectral analysis and compare the results to our simulations. Our conclusions are summarized in Section 6.

2. SOURCE SELECTION

From the catalog of B08, we have selected a subset of the brightest sources ($L_X > 1.2 \times 10^{38}$ erg s^{-1}) within the D_{25} ellipse of the galaxy to perform detailed spectral and temporal analysis. This luminosity cut results in the selection of 12 sources, we further exclude the nuclear source (S81) and the confirmed ultraluminous X-ray source (ULX, S70; Fabbiano et al. 2006), both of which will be the subject of forthcoming papers. We also exclude confused sources in the central region (S75 and S82), where reliable spectral extraction cannot be carried out. This results in a final selection of eight sources. Of these, six lie within the *Hubble Space Telescope* (*HST*) WFPC2 field of view (FOV) of NGC 3379, allowing firm constraints to be placed on their optical counterparts (see B08). Three of these sources (S41, S42, and S67 of B08) are identified with GCs and one has been confirmed as a field LMXB (S86). The other two sources are found within the region of confusion from the *HST* observation (S74 and S77) and are therefore unclassified. The two remaining sources are external to the optical FOV (S102 and S103) and are therefore also unclassified. At a flux of 8.9×10^{-15} erg s^{-1} cm^{-2} (which gives $L_X = 1.2 \times 10^{38}$ erg s^{-1} at $D = 10.6$ Mpc), from the ChaMP+CDF log N–log S relation of Kim et al. (2007), less than 1 source is expected to be a background active galactic nucleus over the area encompassing the eight sources. The $L_X > 1.2 \times 10^{38}$ erg s^{-1} luminosity cut ensures that the selected sources have a minimum of ∼400 counts from the co-added observation and 100 counts in at least one individual observation, allowing meaningful spectral analysis to be carried out. By nature of the selection criteria these sources are either neutron star (NS) binaries emitting near or above the Eddington luminosity, or are BH binaries.

From the observations of NGC 3379 the parameters derived in B08 indicate that BH–LMXBs are present in the X-ray source population of this galaxy, both in the field and in GCs. BH–LMXBs in the field are a well-established class of X-ray binaries in the Galaxy (see the review of Remillard & McClintock 2006, hereafter RM06). Although BH–LMXBs are not expected to be common or luminous in GCs (Kalogera et al. 2004; see Ivanova et al. 2010 for a recent discussion of the formation of BHs within GCs), there is recent convincing evidence of at least two such luminous sources. The first source, a ULX detected within the elliptical Virgo galaxy NGC 4472, exhibits strong X-ray variability (Maccarone et al. 2007; Shih et al. 2008) providing unambiguous evidence for a BH–GC. Subsequent optical spectroscopy of the GC has revealed very broad [O III] emission lines, leading to the suggestion that this source is a stellar-mass BH accreting above or near the Eddington limit (Zepf et al. 2008). The second source, a ULX in NGC 1399 (Irwin et al. 2010), also exhibits strong [O III] emission lines (although these are less broad than the NGC 4472 source) and has little or no hydrogen emission. This source could also be a stellar-mass BH accreting at or near the Eddington limit, although Irwin et al. (2010) suggest that tidal disruption of a white dwarf from an intermediate-mass black hole (IMBH: 100–10^4 $M_\odot$) could explain the optical emission of this GC. From this interpretation a minimum BH mass of 1000 $M_\odot$ is implied. If sources S41, S42, and S67 are luminous BH binaries, the estimated a posterior probability of a BH–GC association is ∼4%, given that 70 GCs are found in NGC 3379 within the joint *Chandra*/Hubble FOV (see B08 and references therein). Given that only 10 GCs are associated with X-ray sources in NGC 3379 (for $L_X >$ a few 10^{36} erg s^{-1}; B08; Kim et al. 2009), these luminous BH–LMXBs may constitute a significant fraction of the GC–LMXB population.

The eight sources presented here are shown in Figure 1, where an adaptively smoothed 0.3–8.0 keV X-ray image is presented, with the source regions and the *HST* FOV overlaid. In Table 1, the log of the *Chandra* observations is reported, along with the background-subtracted net source counts in the 0.3–8.0 keV band, for each source in each observation (as reported in B08). In this table, the optical correlations are also identified, where GC indicates a confirmed GC counterpart, F is a field sources, and - indicates sources with insufficient optical data to confirm a counterpart (or lack thereof).

Figure 2 (adapted from B08) shows the light curves of the eight sources from the *Chandra* observations with panels indicating X-ray luminosity, the hardness ratio (HR) and color values of the source in each observation. In the top panel L_X indicates the X-ray luminosity in the 0.3–8.0 keV band, for an assumed power-law spectrum with $\Gamma = 1.7$ and Galactic line of sight,[13] where the horizontal dashed line indicates the L_X derived from the co-added observation. Because the same

[13] $N_H = 2.78 \times 10^{20}$ cm^{-2} calculated with the tool COLDEN: http://cxc.harvard.edu/toolkit/colden.jsp.

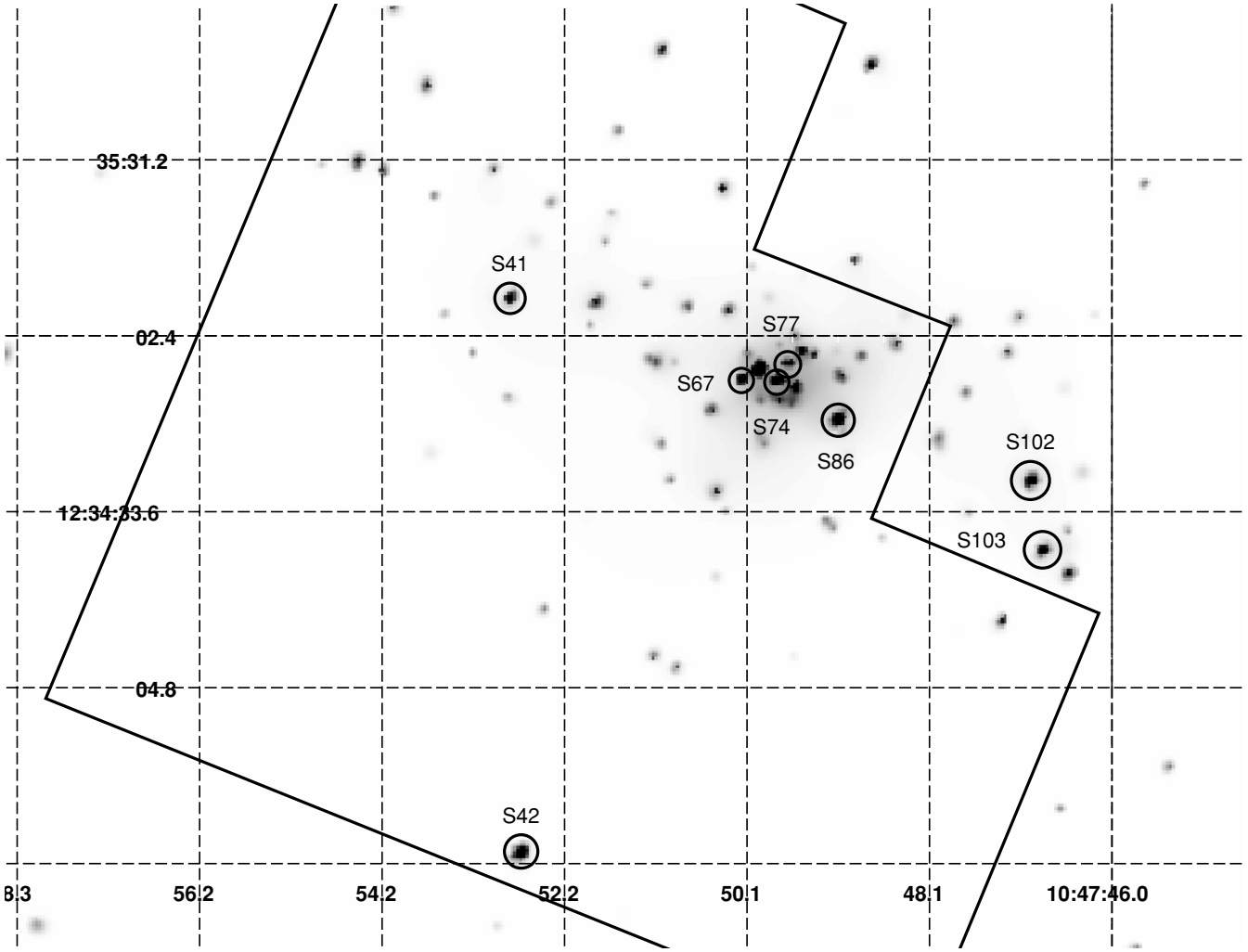

Figure 1. Adaptively smoothed full-band (0.3–8.0 keV) X-ray image of NGC 3379. Overlaid in this figure are labeled circular regions indicating the eight sources presented in this paper and *HST* FOV.

canonical model has been applied to each source this value represents a scaling of the extracted source count rate, where both the spatial and the temporal quantum efficiency variations have been accounted for by generating an energy conversion factor for each sources in each observation (see Section 2.1 in B08 for more details). In the second panel, the HR variation is shown where HR = (Hc-Sc)/(Hc+Sc), with Sc and Hc net counts in the 0.5–2.0 keV and 2.0–8.0 keV bands, respectively. In the third and fourth panels, the X-ray colors C21 and C32 are presented, these colors are defined as C21 = $\log(S_1/S_2)$ and C32 = $\log(S_2/H)$, where S_1, S_2, and H are the net counts, respectively, in the energy bands of 0.3–0.9 keV, 0.9–2.5 keV, and 2.5–8.0 keV. As can be seen from these figures, the eight sources are persistent, in that they were detected with comparable luminosity over a five year span, although the majority exhibits some variability in luminosity and/or spectral properties.

In Table 2, the long- and short-term variability of the sources are summarized, where the short-term variability is defined for each pointing, by means of the Kolmogorov–Smirnov test (K-S test). Here, *V* indicates variable sources (with values >99% confidence), *P* indicates possible variable sources (with variability values >90% confidence), and the "-" indicates non-variable sources. The long-term variability from all five observations was defined by the chi-squared test where *V* indicates variability and *N* indicates a non-variable source. In the last column, *Sign* presents the significance in change in luminosity between the highest and lowest flux observations. All

Table 2
Summary of Long- and Short-term Source Variability

Source No.	Short-term Variability					Long-term Variability	
	Obs 1	Obs 2	Obs 3	Obs 4	Obs 5	Var.	Sign.
S41	-	-	-	-	-	*V*	3.9σ
S42	-	-	-	-	-	*V*	5.9σ
S67	-	-	-	-	-	*N*	1.0σ
S74	*P*	-	-	-	-	*V*	15.8σ
S77	-	-	-	-	-	*V*	2.4σ
S86	-	*P*	-	-	-	*V*	6.0σ
S102	-	-	-	-	-	*V*	10.7σ
S103	-	-	*P*	-	-	*V*	2.0σ

Notes. Individual variability is based on the Kolmogorov–Smirnov test: - indicates no variability, *V* indicates variable source (with values >99% confidence), and *P* indicates possible variable sources (with variability values >90% confidence). The long-term variability from all five observations was defined by the chi-squared test where *V* indicates variability and *N* indicates a non-variable source. Sign indicates the significance in change in luminosity between the highest and lowest flux observations. All of these classification are fully described in B08, Section 2.4.

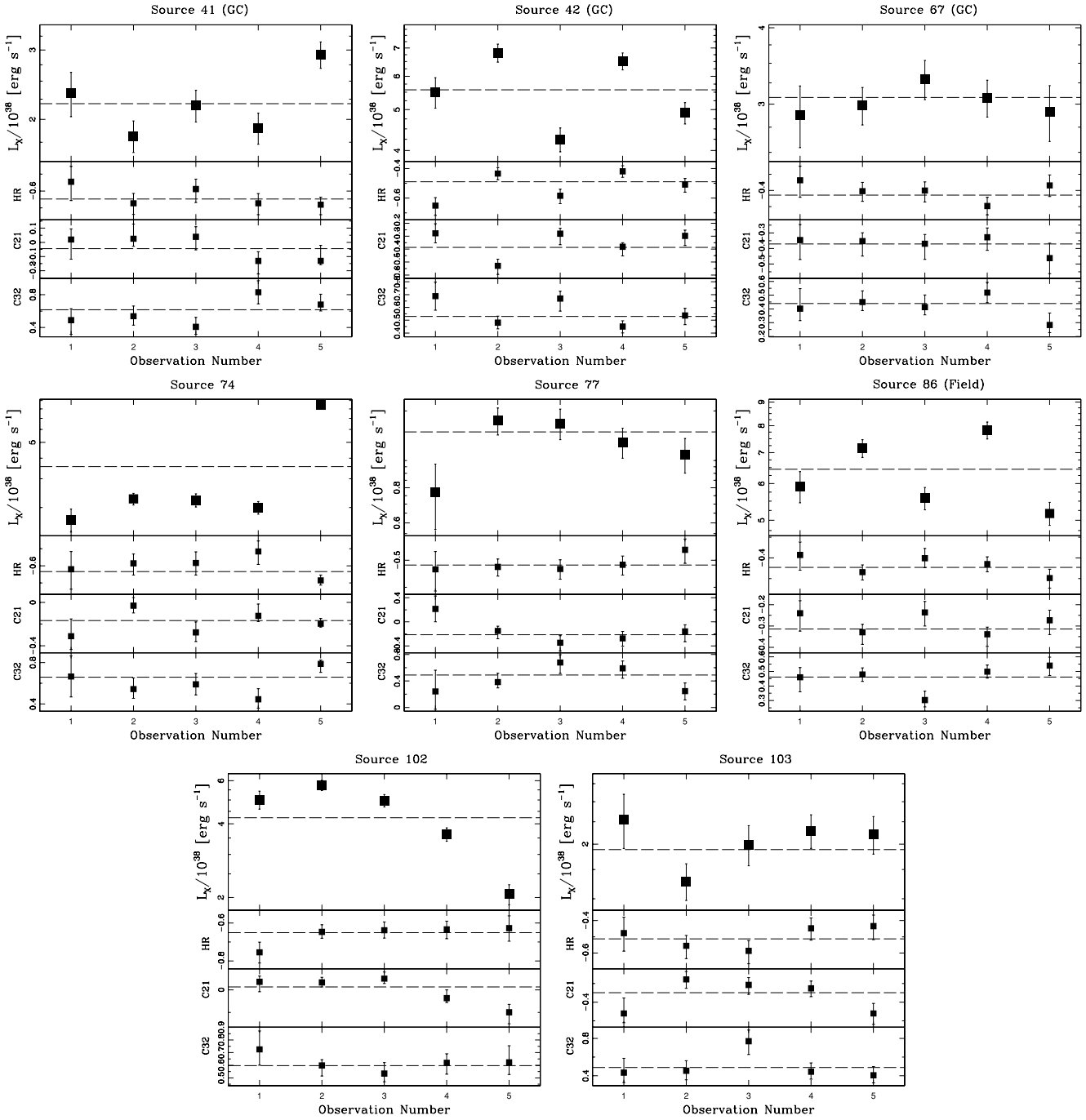

Figure 2. Plots of the eight bright sources in NGC 3379, adapted from B08. Each plot summarizes the variations in properties of each source between each observation. In the main panel, the long-term light curves are shown. In the second panel down, the hardness ratios are indicated. These are defined to be HR $= H - S/H+S$, where H is the number of counts in the hard band (2.0–8.0 keV) and S is the number of counts in the soft band (0.5–2.0 keV). In the third and fourth panels, the color ratios; C21 and C32, are plotted, where C21 $=$ log $S2$+log $S1$ and C32 $= -$log H+log $S2$. For the color ratios the bandwidths are defined to be $S1 = 0.3$–0.9 keV, $S2 = 0.9$–2.5 keV, and H $= 2.5$–8.0 keV. From B08 it was determined that all sources apart from S67 display long-term flux variability.

of these classifications are fully described in B08, Section 2.4. All the sources, with the exception of S67, have been determined to exhibit long-term variability.

3. SPECTRAL ANALYSIS AND RESULTS

The data were processed and calibrated as described in B08. Analysis was performed with the CXC CIAO software suite (v3.4)[14] with CALDB version 3.5 and HEASOFT (v5.3.1). Spectra were extracted for every pointing for each of the eight sources, using the CIAO tool *psextract*, where source regions were defined to be circular regions with radii as in B08; background counts were extracted from surrounding annuli, with outer radii 2–3 times larger, depending on the presence of nearby sources. In cases where the source region was found to overlap with a nearby source, the extractions region radius was reduced and the area of the overlapping source was excluded. The minimum defined extraction radius was 1.″5 on-axis and 3″ off-axis (maximum off-axis angle ∼1.′5), ensuring that the

[14] http://asc.harvard.edu/ciao

Table 3
Summary of the Best-fit Parameters of the Source Spectra

Source	Obs. No.	Net Counts	Model	χ^2/ν	P_{χ^2}	Parameters			$L_X \times 10^{38}$ erg s^{-1}	L_X Range
						$N_H \times 10^{20}$	Γ	kT_{in}	(0.3–8.0 keV)	
S41^{GC}	All	719	PO	25.89/24	0.36	2.8Fr	$1.92^{+0.12}_{-0.11}$	-	2.87	1.99–4.51
S42^{GC}	1 and 3	439	PO	10.32/15	0.79	$17.8^{+4.6}_{-5.0}$	$2.09^{+0.10}_{-0.16}$	-	5.60	4.21–8.15
	1 and 3	439	DBB	12.00/16	0.74	2.8Fr	-	$0.89^{+0.16}_{-0.05}$	4.78	3.18–6.08
	1 and 3	439	DBB	11.32/15	0.73	$0.6^{+2.1}_{-0.6}$	-	$0.97^{+0.13}_{-0.10}$	4.15	3.58–6.55
	2 and 4	971	PO	32.86/40	0.78	$18.8^{+2.6}_{-2.5}$	$1.68^{+0.07}_{-0.10}$	-	12.30	12.22–12.38
	2 and 4	971	DBB	40.05/40	0.47	$3.2^{+2.1}_{-2.1}$	-	$1.50^{+0.16}_{-0.13}$	9.10	7.79–10.76
	5	332	PO	3.85/12	0.98	$12.1^{+4.2}_{-7.5}$	$1.75^{+0.13}_{-0.13}$	-	8.26	7.80–9.60
	5	332	DBB	5.44/13	0.96	2.8Fr	-	$1.21^{+0.12}_{-0.17}$	6.14	3.99–6.94
S67^{GC}	All	1002	PO	31.50/34	0.59	$17.4^{+7.3}_{-6.0}$	$1.57^{+0.17}_{-0.14}$	-	4.48	2.96–5.65
	All	1002	DBB	29.92/35	0.71	2.8Fr	-	$1.55^{+0.11}_{-0.20}$	4.19	2.71–5.16
	All	1002	DBB	29.83/34	0.67	$1.8^{+4.0}_{-1.8}$	-	$1.55^{+0.18}_{-0.17}$	4.67	2.82–5.09
S74	1, 2, 3, and 4	553	PO	16.22/16	0.45	2.8Fr	$1.61^{+0.15}_{-0.14}$	-	2.74	1.51–3.55
	1, 2, 3, and 4	553	DBB	26.39/16	0.05	2.8Fr	-	$1.01^{+0.12}_{-0.18}$	1.95	0.97–2.38
	5	555	PO	35.53/21	0.03	$11.6^{+3.5}_{-4.0}$	$2.13^{+0.11}_{-0.14}$	-	12.39	11.59–13.74
	5	555	DBB	35.68/22	0.03	2.8Fr	-	$0.71^{+0.05}_{-0.05}$	7.65	6.63–7.89
S77	All	368	PO	6.72/7	0.46	$21.9^{+23.9}_{-20.7}$	$2.03^{+0.25}_{-0.42}$	-	1.60	0.37–2.20
			DBB	7.61/8	0.47	2.8Fr	-	$0.98^{+0.21}_{-0.13}$	1.28	0.49–1.71
S86^{F}	1, 3 and 5	920	PO	35.50/37	0.54	2.8Fr	$1.50^{+0.09}_{-0.09}$	-	7.07	6.15–7.95
	2 and 4	1193	PO	39.38/54	0.86	$13.1^{+2.4}_{-2.2}$	$1.65^{+0.10}_{-0.08}$	-	11.82	10.00–13.41
	2 and 4	1193	DBB	42.17/51	0.81	2.8Fr	-	$1.35^{+0.07}_{-0.11}$	9.01	6.73–10.63
S102	1	166	PO	194C	67%C	$3.6^{+4.7}_{-3.5}$	$2.64^{+0.39}_{-0.31}$	-	6.22	5.30–7.07
	2 and 3	792	PO	36.86/32	0.25	2.8Fr	$2.11^{+0.09}_{-0.09}$	-	6.13	5.09–7.03
	2 and 3	792	PO+DBB	20.66/28	0.74	$11.3^{+16.0}_{-11.0}$	$1.62^{+0.18}_{-0.21}$	$0.14^{+0.01}_{-0.02}$	10.78	7.80–11.62
	4 and 5	429	PO	11.84/15	0.69	$2.2^{+4.0}_{-2.2}$	$1.85^{+0.17}_{-0.20}$	-	3.77	2.99–4.73
	4 and 5	429	DBB	28.13/16	0.03	2.8Fr	-	$0.88^{+0.10}_{-0.09}$	0.80	0.33–1.28
S103	All	637	PO	1272C	58%C	$11.6^{+3.3}_{-3.1}$	$1.79^{+0.14}_{-0.13}$	-	3.89	2.88–5.65
	All	637	DBB	1282C	85%C	2.8Fr	-	$1.14^{+0.08}_{-0.09}$	2.78	1.92–3.65

Notes. Errors are given to 1σ. In Column 1 optical correlations (or lack thereof) are indicated by the symbols: GC indicating a GC–LMXB source and *F* indicating that the LMXB has been confirmed as a field source. - indicates that there are insufficient data to establish the presence of an optical counterpart. When the Cash statistic has been used in preference to χ^2 a C is included in Columns 5 and 6. A value of 2.8Fr in Column 7 denotes that the best-fit model has had the absorption column frozen to the Galactic value. Column 11 presents the range in X-ray luminosity where the lowest value indicates the 1σ lower-bound value from the lowest flux individual observation from the joint fit. The higher value indicates the 1σ upper-bound value for the most luminous individual observation from the joint fit. For best fits from individual observations the range indicates the lower- and upper-bound values from that single observation.

source regions enclosed >93% of the encircled energy in all cases.

The source spectra were fitted in XSPEC (v11.3), where the data were restricted to 0.3–8.0 keV, as energies below this have calibration uncertainties, and the spectra presented here do not have significant source flux above 8.0 keV, where the data are highly contaminated by cosmic rays. The spectra were fitted to two models that describe the properties of X-ray binary spectra well (see e.g., review by RM06): the multicolor disk blackbody (DISKBB in XSPEC, hereafter referred to as DBB), and the power law (PO) models, along with the *wabs* photoelectric absorption model.[15] All parameters were allowed to vary freely, although, in cases where the best-fit value of the absorption column N_H was below that of the Galactic absorption, this parameter was frozen to the Galactic value of 2.78×10^{20} cm^{-2}. In instances where there were sufficient counts to bin the data to at least 20 counts per bin (allowing Gaussian error approximation to be used), the minimum χ^2 method was used to fit the data. Where there were too few counts, the Cash statistic (Cash 1979) was used in preference to χ^2, where the spectra were extracted without binning. However, this statistical method has the disadvantage that it does not provide a goodness-of-fit measure like χ^2.

Spectra for each source were first fitted separately for each pointing. These individual best-fit models, alongside the L_X and HR behavior shown in Figure 2, were then used to guide the joint fits for each source. In Table 3, these co-added fits are summarized, where Column 1 gives the source number, Column 2 the observations used in each fit, Column 3 the net source counts, Column 4 indicates which spectral model was used, Column 5 the fit statistic (χ^2 and number of degrees of freedom ν or the C statistics - indicated by C), Column 6 the null hypothesis probability (or goodness when using the Cash statistic). Columns 7–9 present the best-fit values of the fit parameters with 1σ errors for one interesting parameter: N_H (2.8Fr denotes that the value was frozen at Galactic column density), Γ for the PO model, and kT_{in} the temperature of the innermost stable orbit of an accretion disk, for the DBB. Column 10

[15] Given the statistics of our data and the ACIS resolution, use of other absorption models does not affect our results and conclusions (see Section 4.3).

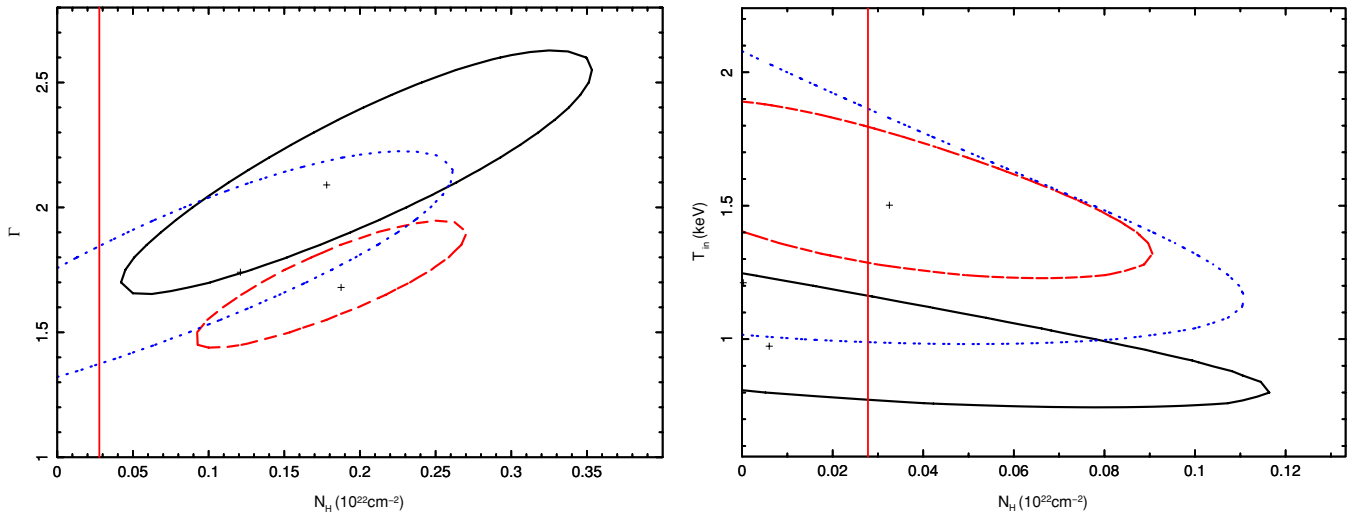

Figure 3. Contours for PO (left) and DBB fits (right) for S42. In both figures, the black solid line represents the 2σ contour for observations 1 and 3, the red dashed line observations 2 and 4, and the blue dotted line observation 5. Best-fit values are indicated by the cross hair within each contour (these values differ from the best-fit parameters presented in Table 3 when $N_{\rm H}$ is below Galactic absorption). In some instances cross hairs are not readily observable, in these cases the best-fit value of $N_{\rm H}$ tended to 0 when left free to vary. The solid vertical line indicates Galactic $N_{\rm H}$. From the simulations presented in Section 4, the spectral properties of S42 suggest that this source is predominately in a thermally dominant state, entering an intermediate state in observation 5 (see the text for details).

(A color version of this figure is available in the online journal.)

indicates the intrinsic value of $L_{\rm X}$ (calculated as a weighted average of the individual luminosities from the joint fit) and Column 11 the source luminosity range. This range was taken from the (1σ) lower-bound value of the lowest flux observation included in the joint spectral fit, to the (1σ) upper-bound value of the highest flux observation included in the joint fit. When only one spectrum was modeled, the range indicates the lower- and upper-bound $L_{\rm X}$ values from that single observation.

3.1. Globular Cluster Sources

Of the sub-sample of sources presented in this paper, three have been determined to be GC–LMXBs. Through inspection of their $L_{\rm X}$, HR and color values presented in Figure 2, and the individual spectral fits of each source, two LMXBs (S41 and S67) have been determined to exhibit little flux and no spectral variability, while the remaining source (S42) has been found to exhibit spectral changes between each observation, with a variance in flux significance of 6σ. In the case of the non-varying LMXBs, the five spectra for each source were jointly fitted in XSPEC, where all parameters, apart from the normalizations, were linked. For both sources the DBB and PO models were fitted to the spectra, these best fits are summarized in Table 3. In cases where the DBB model was statistically rejected the PO model only is presented.

For the variable source, S42, the most luminous GC–LMXB in our sample, the individual fits and $L_{\rm X}$ and HR values from B08 indicate that the source has been observed in three different spectral states. The spectra have therefore been grouped to reflect these differences. The first grouping contains spectra with lower $L_{\rm X}$ and soft HR value (obs 1 and 3), the second spectra with higher $L_{\rm X}$ and hard HR value (obs 2 and 4), and the remaining spectrum indicates an intermediate state (obs 5). Both the DBB and PO models were applied to these three joint fits and are summarized in Table 3. The 95% confidence contours for two interesting parameters are presented in Figure 3 where the left-hand panel shows the PO model in the three spectral groups and right-hand panel the DBB fits. In both panels Galactic $N_{\rm H}$ is indicated by the vertical solid line.

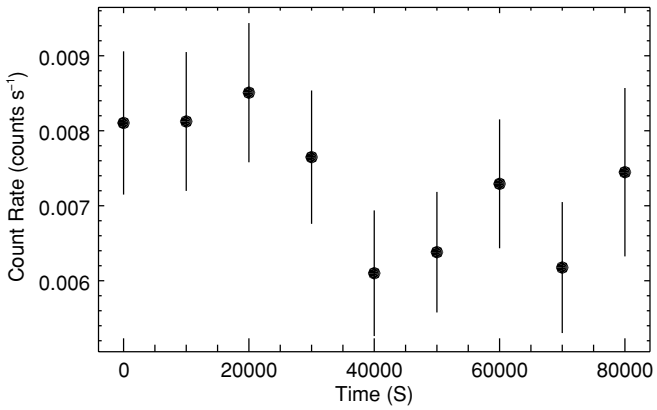

Figure 4. Short-term light curve of S86 from observation 2. The *x*-axis provides time in seconds, beginning from the start of the observation, and the *y*-axis provides count rate in counts s^{-1} between 0.3 and 8.0 keV. Binning of 10,000 s was used when extracting counts to provide adequately constrained count rates to identify variability.

3.2. The Field Source

Only one source presented in this paper has been confirmed as a field LMXB, S86. It has been determined that this source not only exhibits long-term variable behavior in both its flux and spectra, but that it also displays short-term flux variability (defined as a possible variable source with the K-S test: Table 2) during the second pointing. This short-term variability has been further investigated through examining the light curve of the source during observation 2, which was created with the CIAO tool *dmextract*. To provide well-constrained values of count rate, allowing variability to be identified, binning of 10,000 s was used when extracting counts. This resulting light curve is shown in Figure 4, where it can be seen that the count rate drops from ~0.008 counts s^{-1} to ~0.006 counts s^{-1} part-way through the observation. Spectra were extracted from these two different count-rate epochs, to identify if a change in spectral shape accompanied this change in flux, however, it was determined that, within errors, the best-fit values from the two spectra were identical.

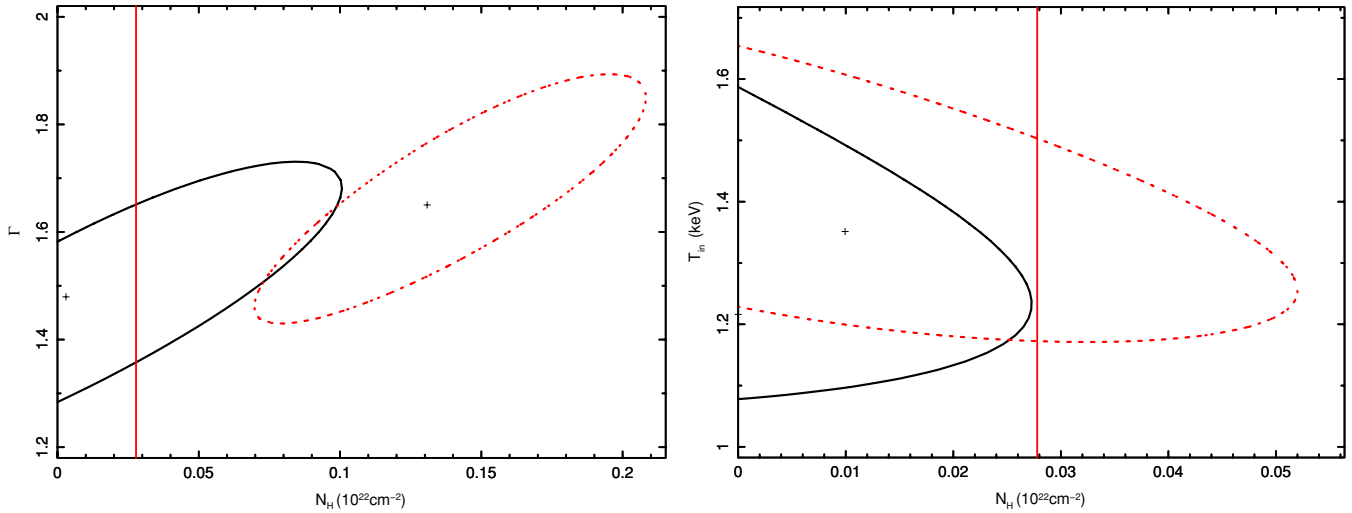

Figure 5. Contours for PO (left) and DBB fits (right) for S86. In both figures, the black solid line represents the 2σ contour for observations 1, 3, and 5, the red dotted line observations 2 and 4. Best-fit values are indicated by the cross hair within each contour (these values differ from the best-fit parameters presented in Table 3 when $N_{\rm H}$ is below Galactic absorption). In some instances cross hairs are not readily observable, in these cases the best-fit value of $N_{\rm H}$ tended to 0 when left free to vary. The solid vertical line indicates Galactic $N_{\rm H}$. From the simulations presented in Section 4 the spectral properties of S86 indicate that this source is transitioning between a hard state (or possibly a cool-disk state) to a thermally dominant state (see the text for details).

(A color version of this figure is available in the online journal.)

Once it had been determined that the short-term variability of S86 did not correspond to any spectral variation, the long-term spectral variability was investigated. Once again, guided by the individual spectral fits and the X-ray luminosity and HR values, the spectra were separated into two groups; a low $L_{\rm X}$ hard HR state (1, 3 and 5) and a high $L_{\rm X}$ softer HR state (2 and 4). These best-fit values are summarized in Table 3 and their confidence contours are presented in Figure 5.

3.3. Unclassified Sources

The remaining four sources in this paper have insufficient optical data to confirm them as field or GC sources, either residing with the central 5″ of the galaxy, where source confusion means GC sources cannot be easily identified or are detected outside of the *HST* FOV. Of these sources, two (S77 and S103) have been determined to have no spectral variability, despite both of them being classified as having flux variability. Consequently all five observations were fitted jointly for each source, following the methods described in Section 3.1 for S41 and S67.

Of the two remaining LMXBs (S74 and S102), both have been determined to have variability and require separate spectral modeling. S74 exhibits stable long-term flux and spectra over the first four observations but in observation 5 a four-fold increase in flux (with a significance in flux change of 16σ) and a softening in HR is observed. The joint fits have therefore been separated into observations 1, 2, 3, and 4, and observation 5, to reflect these variations. When modeling the spectrum from observation 5 it was found that there was a drop in count rate in the binned data at $\sim$1.15 keV and from additional analysis it was determined that this feature was still present in the unbinned data. To further investigate this, additional components were included in the spectral model in an attempt to describe this feature. However, no physical models described the data well. Background subtraction, edge effects, and calibration uncertainties were also considered as an explanation of the low energy bin but after further investigation all were rejected. After ruling these possibilities out, the most likely remaining explanation of this "feature" is that it is a consequence of statistics, and not a physical feature of the source. The PO and DBB models were fitted to the whole of the 0.3–8.0 keV spectrum and these best-fit model parameters are presented in Table 3. In subsequent fits, the energy range of 1.1–1.2 keV was excluded to determine the effect of the low-count bin. From this it was shown that the best-fit values are consistent with those from the full spectrum fit, although the goodness-of-fit values are greatly improved by excluding this energy range (PO χ^2/ν from 1.69 to 1.30; DBB χ^2/ν from 1.62 to 1.26). Some short-term (possible) variability was also observed in observation 1 of S74, although there are too few counts in this pointing to be able to further investigate this.

Through inspection of not only the long-term light curve and HR values of S102 (Figure 2) but also its individual fits, there is a suggestion of a gradual and continual change in flux. Initially this is an increase in flux from the archival observation to the more recent pointings, followed by a steady decline, which is coupled with a suggestion of hardening in HR values. Therefore, the joint fits were divided into three groups. Observation 1, the softest HR value, observations 2 and 3, high $L_{\rm X}$, and observations 4 and 5, lower $L_{\rm X}$. As with the previous sources, single-component PO and DBB models were applied to the spectra.

However, for group 2, when the source count rate is at its highest, the best-fit values from the PO model did not provide physically realistic parameters where the best-fit value of $N_{\rm H}$ was significantly below Galactic $N_{\rm H}$, therefore a composite DBB+PO model was applied to the data.

The best-fit spectra of these four sources are all summarized in Table 3 and the confidence contours of S74 are presented in Figure 6. The confidence contours from the single-component PO model of the three spectral groupings from S102 are presented Figure 7 and the contours from the two-component model of observations 2 and 3 are shown in Figure 8.

4. SIMULATIONS OF LMXB SPECTRA

From studies of Galactic binaries it has been observed that the energy spectra of LMXBs often exhibit a composite shape

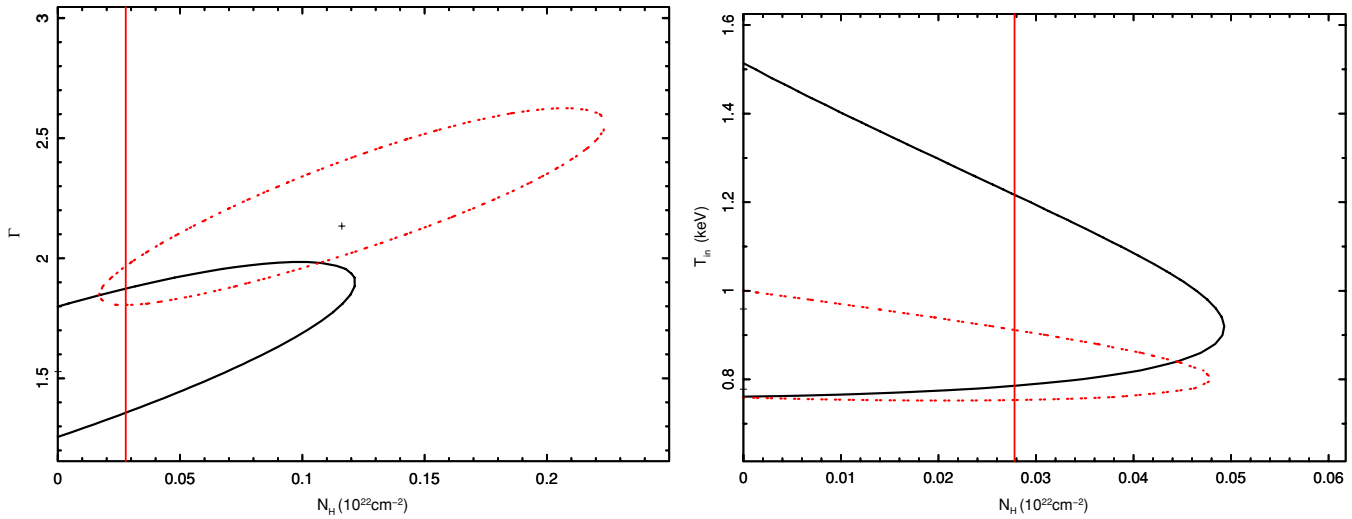

Figure 6. Contours for PO (left) and DBB fits (right) for S74. In both figures, the black solid line represents the 2σ contour for observations 1–4, the red dotted line observations 5. Best-fit values are indicated by the cross hair within each contour (these values differ from the best-fit parameters presented in Table 3 when $N_{\rm H}$ is below Galactic absorption). In some instances cross hairs are not readily observable, in these cases the best-fit value of $N_{\rm H}$ tended to 0 when left free to vary. The solid vertical line indicates Galactic $N_{\rm H}$. Based on the simulations presented in Section 4, S74 is likely to be in a hard state in observations 1–4, transitioning to a thermally dominant state in observation 5 (see the text for details).

(A color version of this figure is available in the online journal.)

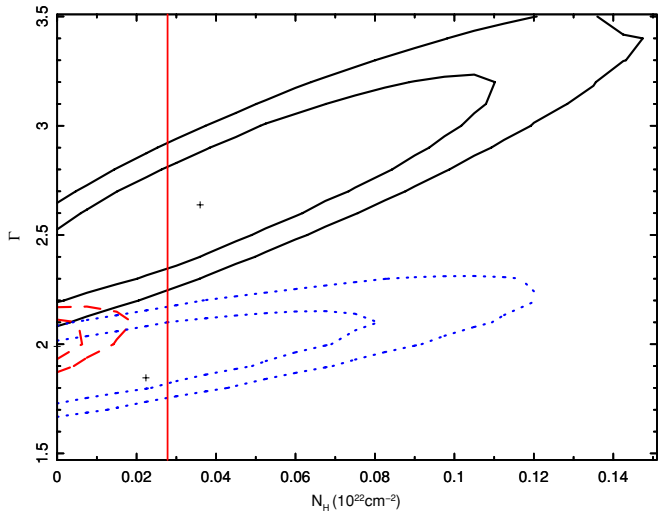

Figure 7. 1σ and 2σ contours for the PO best fit for S102. The solid black lines represent contours for observation 1, the red dashed lines show contours for observations 2 and 3, and the dotted blue lines observations 4 and 5. Best-fit values are indicated by the cross hair within each contour (these values differ from the best-fit parameters presented in Table 3 when $N_{\rm H}$ is below Galactic absorption). In some instances cross hairs are not readily observable, in these cases the best-fit value of $N_{\rm H}$ tended to 0 when left free to vary. The solid vertical line indicates Galactic $N_{\rm H}$. From the simulations presented in Section 4, S102 is likely to initially be in a steep power-law state, transitioning to a luminous cool-disk state in observations 2 and 3 and then changing to a hard state in observations 4 and 5 (see the text for details).

(A color version of this figure is available in the online journal.)

of both thermal and non-thermal emission components. In these sources, the thermal component is well modeled by the multicolor disk blackbody model, which originates in the inner accretion disk, and the non-thermal component is well described by a power-law component. This composite emission provides a wide range in X-ray properties that can be classified into five distinct spectral states. In RM06, these states are defined to be; the quiescent state, a non-thermal hard state with very low emission ($L_{\rm X}$ $10^{30.5}$–$10^{33.5}$ erg s^{-1}), the hard state (denoted hereafter as NT; non-thermal state, to avoid confusion with the high/soft state classification that can also be used to describe LMXB spectral states), where the non-thermal component dominates the spectra (>80%[16]) and the spectral index is in the range $1.5 < \Gamma < 2.1$, and the thermally dominant (TD) state, where the thermal emission arising from the disk contributes to more than 75% of the flux. In the TD state, the disk temperature is typically in the range of 0.7–1.5 keV and the faint power-law component is steep ($\Gamma > 2.1$). Sources have also been observed in the steep power law (SPL) state, where the sources are much brighter ($L_{\rm X} > 0.2L_{\rm Edd}$) with a significant flux contribution arising from the non-thermal component with a steeper slope of >2.4, compared to ∼1.7 in the hard state. The final spectral class encompasses emission not defined by the other states, where spectra appear to show sources between states, this is termed the intermediate state. It should be noted that this definition does not represent a single state but indicates that the source emission cannot be described by any of the four previous source classes.

From *Chandra* and *XMM-Newton* observations of extragalactic LMXBs there are typically too few counts to apply composite models to each spectrum, therefore single-component models that provide an approximation of the spectra must be applied to the data. To understand how well these single-component models describe the X-ray emission of LMXBs, simulations have been performed with Sherpa (v3.4), using *Chandra* response files. In these simulations, spectra have been produced from two-component models comprising both a multicolor disk (XSDISKBB in Sherpa; the XSPEC DBB model used in Section 3) and a PO component, along with the *phabs* photoelectric absorption model which has a value of Galactic absorption. This model covers the 0.3–8.0 keV *Chandra* energy range. These generated spectra have then been fitted to single-component models to characterize the typical best-fit values that are recovered. To

[16] Where the full-band flux is 2–20 keV from *RXTE* spectra, not the 0.3–8.0 keV band that has been used in the rest of this paper. Although, definitions from RM06 do provide a fairly accurate interpretation of spectral states observed in the *Chandra* bandpass.

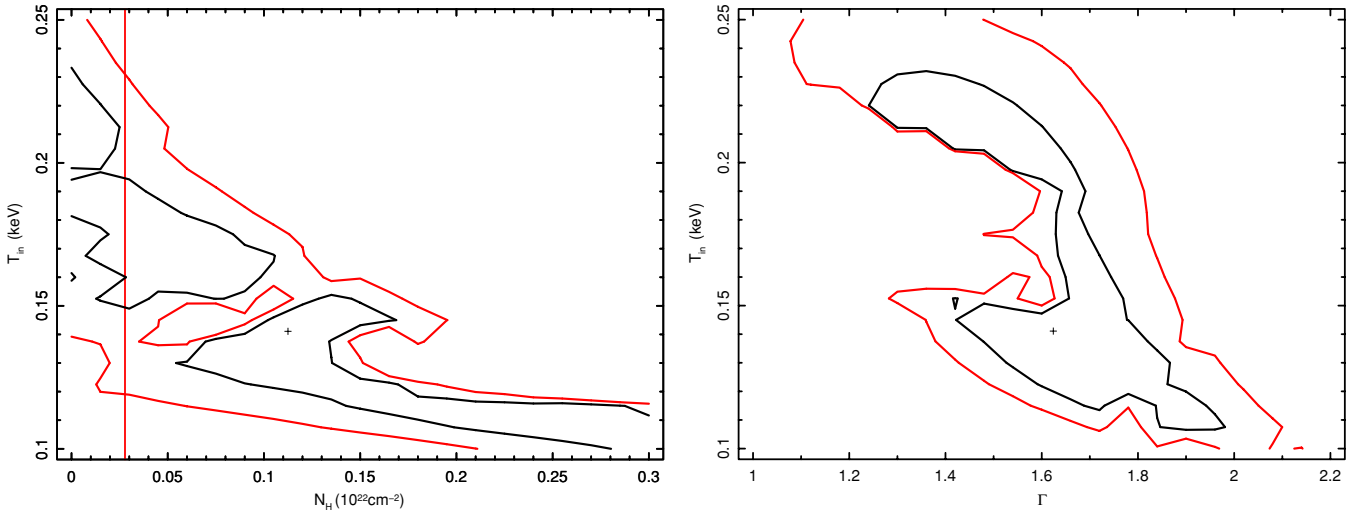

Figure 8. 1σ and 2σ contours for the two-component PO+DBB modeling of observations 2 and 3 of S102. Left indicates values of $N_{\rm H}$ and $kT_{\rm in}$ and the right panel presents the Γ and $kT_{\rm in}$ values from the same fit. The best-fit values are indicated by the cross hairs in both panels. In the left panel, the solid vertical line indicates Galactic $N_{\rm H}$.

(A color version of this figure is available in the online journal.)

broadly cover physical properties that have been observed in the spectra of Galactic LMXBs (RM06) simulations were run over a large parameter space where the inner-disk temperature of the DBB model ranged from 0.50 keV to 2.25 keV in steps of 0.25 keV and input Γ slopes increased in steps of 0.2, from 1.5 to 2.5. Further, to investigate how the composite spectral shape of sources in hard, TD, and SPL states were represented by single-component fits, different flux ratios of 75%, 60%, 50%, 40%, 25%, 10%, and 0% were also included in the simulations, where the percentage indicates the flux contribution from the thermal component. This was also expanded to include a subset of parameters at 90% and 100%, where spectra with Γ fixed at 1.7 and 2.5 were produced for the full disk temperature range. It was necessary to produce only a subset of these flux-ratio values due to the computer intensive nature of these simulations. A value of 2.5 was selected for Γ based on typical LMXB photon index values of sources in a TD state. A photon index of 1.7 was selected based on the results from the lower flux-ratio simulations, where this input parameter was found to provide median values of $N_{\rm H}$, Γ, and $kT_{\rm in}$ for the single-component best-fit parameters over the full photon index range.

To replicate the quality of data that has been presented in this paper, the generated models were scaled to produce spectra of 1000 counts, with subsequent runs also covering a subset of 500 and 250 count data. After a spectrum was generated in Sherpa, using the *fakeit*[17] command, single-component PO and DBB models were fitted and the best-fit values recorded. Following this, the original two-component model was fitted to the data to ascertain how reliably the low-count spectrum could recover the input parameters. For each set of parameters 100 spectra were generated, providing a measure of the standard deviation of the best-fit values.

4.1. Single-component Spectra

4.1.1. Single PO Fits

In Figure 9, a summary of the results of fitting the single-component PO model is presented. In the left-hand panel, the best-fit value of $N_{\rm H}$ for each of the parameter models is shown and in the right-hand panel the difference (Δ) between input and best-fit photon index is presented. In both panels, the best-fit values are plotted against increasing thermal flux ratios, with the solid diagonal lines indicating the best-fit values for $\Gamma = 1.7$, for each temperature step of the disk component (a subset of temperatures is shown for clarity in the figure). The shaded regions indicate the maximum and minimum values of $N_{\rm H}$ over the full photon index range for each temperature step (where only photon index values of 1.7 and 2.5 have been simulated for flux-ratio values of 90% and 100%). In the left-hand panel, the horizontal dashed line indicates the value of Galactic $N_{\rm H}$ for NGC 3379. The standard deviations for the 1000 count spectra for the 75% and 25% flux ratios are indicated by the error bar in the top left corner of the plot, where the smaller error bar indicates the 25% flux-ratio standard deviation ($\sigma = 1.82 \times 10^{20}$ cm^{-2}) and the larger error bar the standard deviation from the 75% flux-ratio model ($\sigma = 3.30 \times 10^{20}$ cm^{-2}).

From these figures it is clear that as the spectra become more disk dominated the best-fit values from the single-component PO model increasingly diverge from the input parameters of the two-component model. Importantly, for all values of $kT_{\rm in}$ and Γ, best-fit values of $N_{\rm H}$ are above Galactic (excepting the spectra generated from the extreme models with input parameters $\Gamma = 2.3$–2.5 and $kT_{\rm in} \geqslant 1.50$ keV) and even up to $\sim$8 times that of Galactic when the spectra are in a TD state (i.e., the disk fraction contributes more than 75% of the total flux). In fact, assuming a typical disk temperature of 1 keV, even with a disk contribution of only 40% the recovered $N_{\rm H}$ from the single-component PO fit is >3 times Galactic $N_{\rm H}$ (a value significantly above the Galactic value even after considering the standard deviation). Further, unsurprisingly, the difference between the input and best-fit photon index ($|\Delta\Gamma|$) increases as the ratio of disk flux to total flux increases, indicating that, as the non-thermal component becomes less prominent within the composite fit, the reliability of the Γ recovered from the single-component model is reduced.

A subset of these simulations was also generated for spectra with 500 and 250 counts, where flux-ratios models of 100%, 90%, 75%, 60%, 50%, 25%, and 0% were produced with an inner-disk temperature of 1 keV and a photon index of 1.7.

[17] http://asc.harvard.edu/sherpa3.4/threads/fakeit/

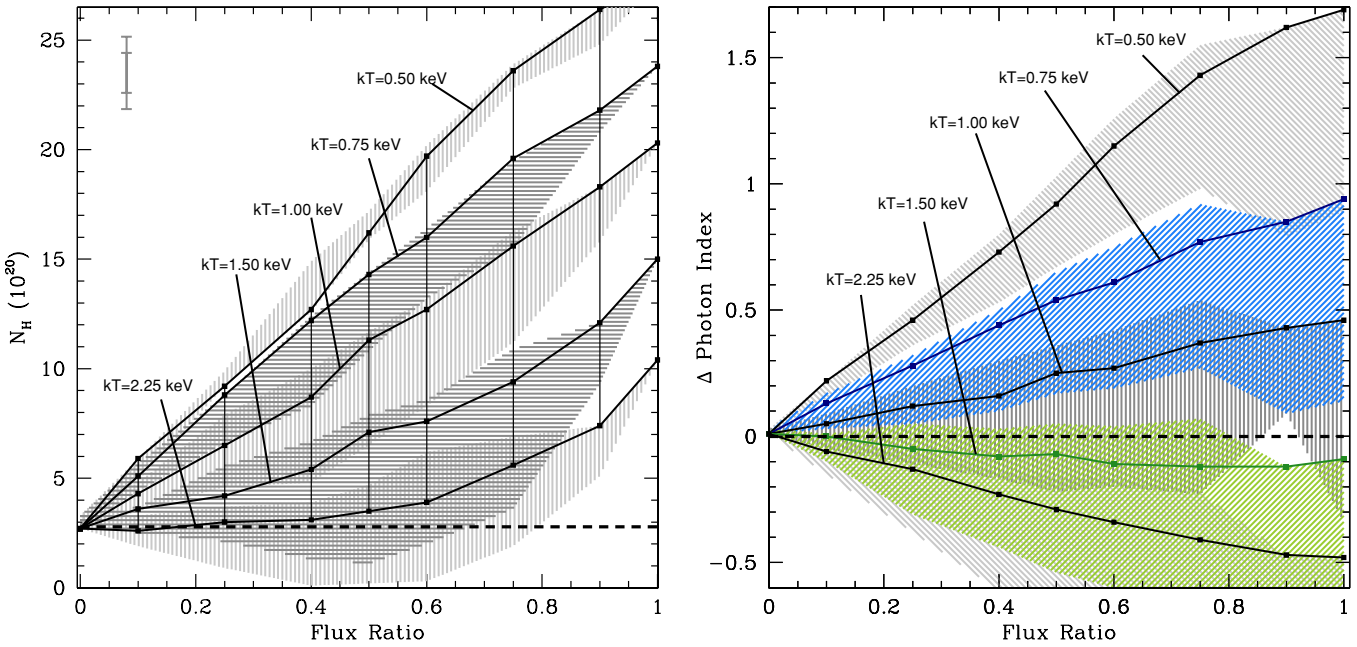

Figure 9. Results of the best-fit values derived from the single-component PO model applied to the 1000 count simulated spectra (detailed in Section 4), where all spectra were simulated with Galactic $N_{\rm H}$. The left panel indicates the values of $N_{\rm H}$ plotted against the flux ratio of the disk-to-total flux. The right panel shows the difference (Δ) between the input and best-fit value of Γ. In both plots, the solid diagonal lines label input $\Gamma = 1.7$ for each simulation, for input $kT_{\rm in}$ values of 0.50, 0.75, 1.00, 1.50, and 2.25 keV. The shading indicates the spread in best-fit values for the full range of photon indices 1.5–2.5. In the left panel, the horizontal dashed line indicates the Galactic $N_{\rm H}$ and the vertical solid lines are grid line. The error bars in the upper left corner indicate the standard deviation of the 0.75 (large) and 0.25 (small) value of $N_{\rm H}$. In the right panel, the $kT_{\rm in}$ values are presented in different colors for clarity. It should be noted that different shading patterns of green, blue, and gray are a consequence of overlapping shading and do not indicate additional information within the figure.

(A color version of this figure is available in the online journal.)

In addition, for the higher flux-ratio values $\geqslant$60%, models with $\Gamma = 2.5$ were also used as input parameters for the simulations to represent TD states. The best-fit values of $N_{\rm H}$ with lower count spectra are compared with the full 1000 count simulations in Figure 10, where the 1000 count spectral results are presented in an identical manner to the left-hand panel of Figure 9. The best-fit $N_{\rm H}$ values of the 500 and 250 count spectra are indicated by the blue and green lines, respectively, with the shading indicating the best-fit values from the $\Gamma = 2.5$ simulations. As in Figure 9, the standard deviations of the 75% and 25% flux ratios are indicated by the color-coded error bars in the top left corner of the plot. From this figure it is clear that despite the larger standard deviations in the lower-count models, the best-fit values of $N_{\rm H}$ are almost identical to those obtained with the 1000 count data. Even in the case of 250 counts, when an LMXB is in a "typical" thermal-dominant state (i.e., $kT_{\rm in} = 1$ keV, $\Gamma = 2.5$, and disk flux >75%) the best-fit value of $N_{\rm H}$ is still more than three times that of Galactic absorption.

4.1.2. Single DBB Fits

A summary of fitting the single-component multicolor disk models from the simulations is presented in Figure 11. In the left-hand plot of this figure, the $N_{\rm H}$ values from the DBB model with a fixed PO component of $\Gamma = 1.7$ are plotted for disk temperatures 0.50 keV, 0.75 keV, 1.00 keV, 1.50 keV, and 2.25 keV. No shading is shown for the different photon index slopes in this panel due to the small deviations in best-fit values of $N_{\rm H}$. Galactic $N_{\rm H}$ is indicated by the dashed horizontal line. In the right-hand panel $\Delta kT_{\rm in}$ is shown against increasing flux ratios, where the variation of best-fit $kT_{\rm in}$ for different values of photon index is indicated by the shaded regions. The $\Gamma = 1.7$ input parameter values are shown by the solid lines.

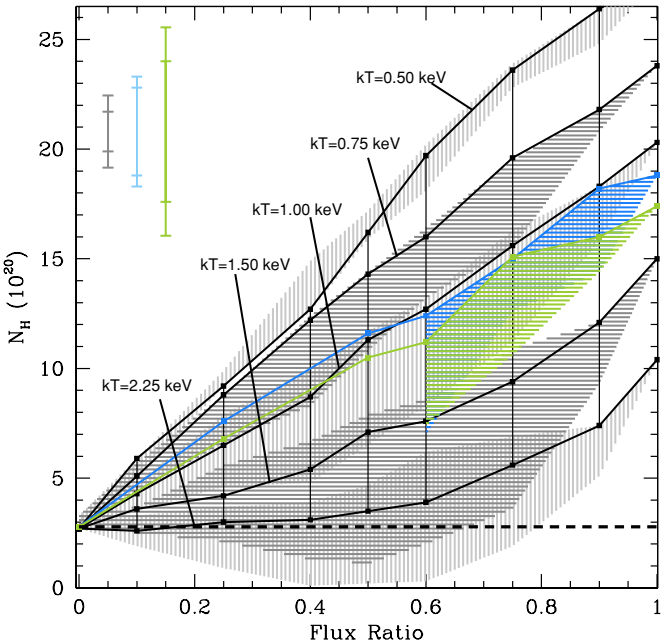

Figure 10. Same information as is shown in the left panel of Figure 9 but also includes the best-fit values of $N_{\rm H}$ derived from lower count simulations of input parameters $\Gamma = 1.7$ and 2.5 and $kT_{\rm in} = 1.00$. The 500 count data are plotted in blue and the 250 count data in green. The results of the $\Gamma = 1.7$ simulations are labeled by the solid diagonal lines and the best-fit values of $N_{\rm H}$ from the $\Gamma = 2.5$ simulations for 60%, 75%, 90%, and 100% disk-to-total flux ratios are indicated by the outer edge of the shading (following the findings of the 1000 counts simulations, intermediate values of Γ are expected to reside within the shaded region). Error bars in the top left indicate the standard deviation for 0.75 (large) and 0.25 (small) flux ratios, these are also color coded. The horizontal dashed line indicates Galactic $N_{\rm H}$.

(A color version of this figure is available in the online journal.)

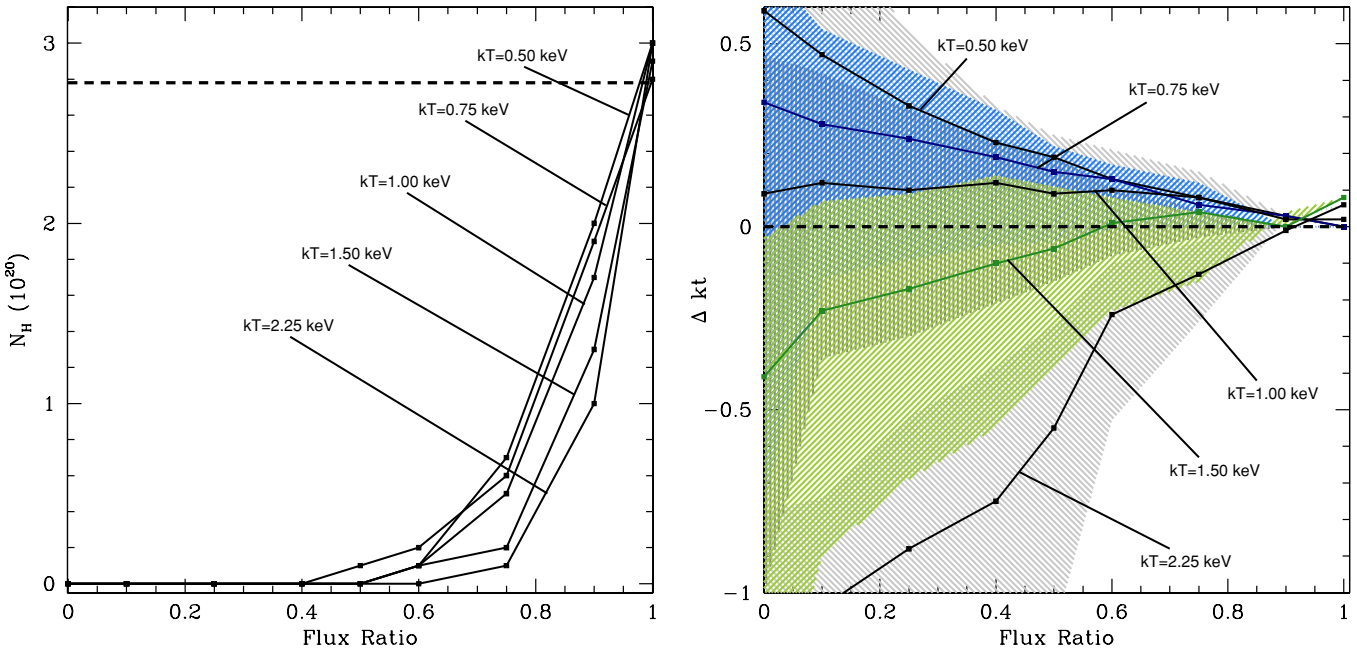

Figure 11. Best-fit values derived from the single-component DBB model applied to the simulated spectra with input values of $N_{\rm H}$ set to Galactic absorption (detailed in Section 4). As in Figure 9, the left panel indicates the values of $N_{\rm H}$ plotted against the flux ratio of the disk-to-total flux and the right panel shows the difference (Δ) between the input and best-fit value of $kT_{\rm in}$. In both plots, the solid diagonal lines label input $\Gamma = 1.7$ for each simulation, for input $kT_{\rm in}$ values of 0.50, 0.75, 1.00, 1.50, and 2.25 keV. Shading is not presented in the left panel due to the small variations of output $N_{\rm H}$ values but in the right panel it indicates the spread in best-fit values for the full range of photon indices 1.5–2.5. It should be noted that different shading patterns of green, blue, and gray are a consequence of overlapping shading and do not indicate additional information within the figure. The Galactic absorption column is indicated in the left panel by the horizontal dashed line.

(A color version of this figure is available in the online journal.)

From these figures it can be determined that when the flux emission does not arise entirely from the disk component of the LMXB, the best-fit value of $N_{\rm H}$ from the single-component DBB model is < Galactic absorption. In fact, even with a thermal flux ratio of 75% the best-fit value of absorption is more than three times smaller than that of Galactic, tending to 0 as the flux ratio decreases. In the right-hand panel, it is shown that as the input parameters of the simulations generate lower flux-ratio spectra, so the value of $|\Delta kT_{\rm in}|$ increases. This indicates that as the composite model becomes more dominated by the non-thermal component the best-fit parameters from the DBB model become less reliable, as was seen with the single-component PO model for the disk-dominant spectra.

4.1.3. Composite PO+DBB Fits

In addition to the single-component fits, a composite PO and DBB model, with initial parameters set to the input values of the simulation, was also applied to each of the spectra. In all cases the fit was statistically acceptable, however, by comparing the best-fit values to the input parameters the two-component model was unable to adequately recover the initial values. This is due to the degenerate nature of the disk and PO components of the model and indicates that, in general, for sources with less than 1000 counts a two-component model will be unable to provide well-constrained parameters (although this will be dependant on the shape of the spectrum).

4.1.4. $N_{\rm H}$ as a Discriminate

These simulations provide a robust framework in which low-count single-component spectra can be used to infer properties of LMXBs and their spectral state. From these spectra it has been demonstrated that, while PO or DBB models are not capable of accurately constraining the spectral parameters of X-ray binaries when both a strong thermal and a non-thermal component are present in the spectrum, they can provide important information that can be used to aid the interpretation of the source's spectral state. From the single-component PO model, the $N_{\rm H}$ parameter is a strong indicator of the flux ratio between the two spectral components, where an elevated value of intrinsic absorption is indicative of the source containing a significant disk component (of at least 25% flux for lower inner-disk temperatures). In fact, this thermal to non-thermal contribution can be further constrained by determining the $N_{\rm H}$ absorption value from the DBB fit, where only sources in a TD state provide values that are consistent with Galactic $N_{\rm H}$. Further, these simulations have also determined the reliability of the photon index or $kT_{\rm in}$ values recovered from the single-component models for these composite sources. In the case of the PO model, when the source is in a hard state, indicated by a value consistent with Galactic $N_{\rm H}$, the best-fit value of Γ provides an accurate value of the input parameter. Similarly, when the best-fit value of $N_{\rm H}$ from the DBB model provides values > 0, indicating the source is in a TD state, the best-fit $kT_{\rm in}$ provides a reliable value of the true inner-disk temperature. In all other instances, neither models provide a reliable measure of the intrinsic source properties.

4.1.5. Flux Determination

In addition to the Γ, $kT_{\rm in}$, and $N_{\rm H}$ parameters, 0.3–8.0 keV values of flux from the single-component models were also compared to the input flux values. A comparison of the derived fluxes for disk temperatures of 0.50, 1.00, and 2.25 keV, and photon index values 1.7 and 2.5 are shown in Figure 12. In this figure the fluxes from the three different models, as well as a canonical PO model of Galactic $N_{\rm H}$ and $\Gamma = 1.7$, are show in six panels, where the left-hand panels indicate fluxes for all values

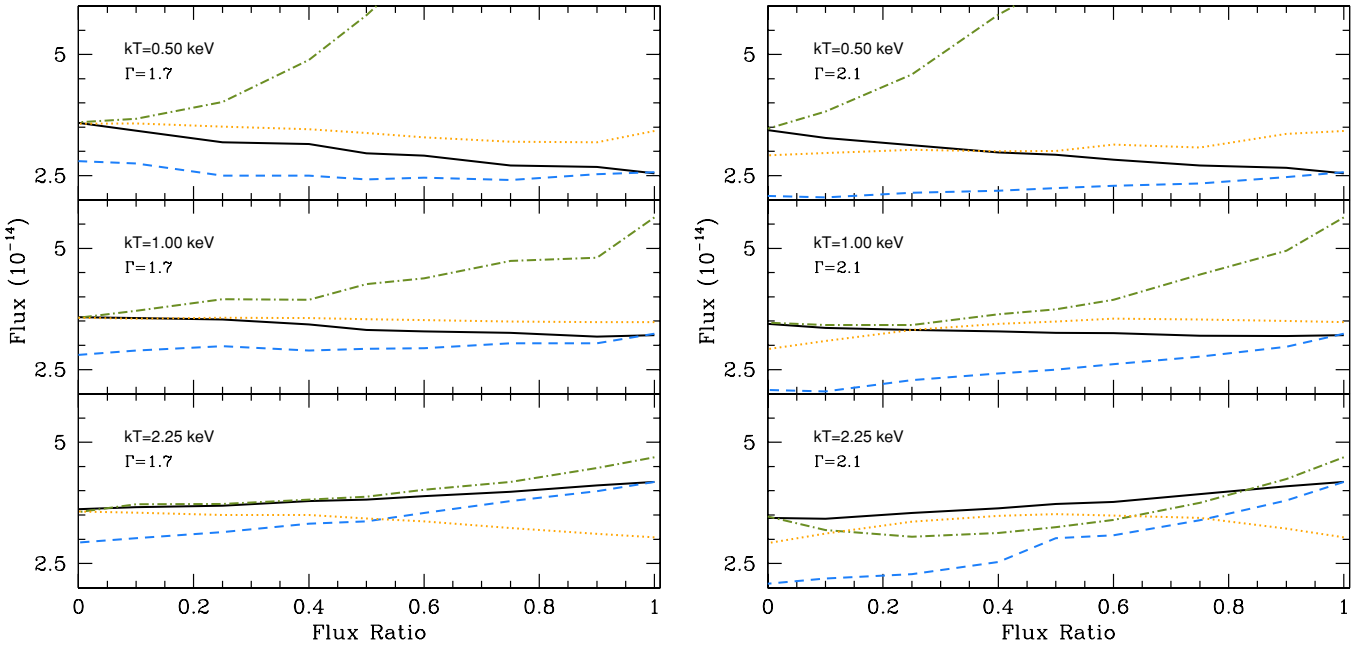

Figure 12. L_X plotted against the flux ratio, where the 0.3–8.0 keV flux from the input two-component PO+DBB model (black line) is compared to the L_X values derived from the single-component fits; the PO model is indicated by the dash-dotted green line and the DBB model by the dashed blue line. Flux derived from a canonical PO model of Galactic N_H and $\Gamma = 1.7$ is indicated by the dotted orange line. The panels on the left indicate the simulations with an input $\Gamma = 1.7$ and on the right the $\Gamma = 2.1$ simulations. Input kT_{in} values are labeled in each panel, as is the input photon value.

(A color version of this figure is available in the online journal.)

of kT_{in} from the $\Gamma = 1.7$ models, and the right-hand panels present the flux values from the $\Gamma = 2.5$ models. The fluxes derived from the composite models are indicated by the solid black lines, the single PO model by the dot-dashed green lines, the best-fit values from the DBB model the dashed blue lines, and the canonical model flux is indicated by the dotted orange line.

From this figure it can be seen that as the disk component becomes more prominent in the composite model, the value of flux derived from the single-component PO model diverges from the flux determined from the composite model. The value of this divergence increases as the temperature of the inner disk decreases. Further, by comparing these changes in flux with Figure 9 it can be seen that in all instances where an elevated value of N_H is determined from the PO model, the intrinsic flux from the fit is significantly higher than the true source value, a consequence of the excess soft emission of the disk being modeled by the higher absorption component. Conversely, the intrinsic flux from the DBB best-fit model shows a lower value than the one defined by the input model in all instances, up to a disk contribution of 100%. Although, these lower values provide a much closer value to the true flux than that provided by the single-component PO fit (for instances where absorption column values above Galactic N_H are recovered). However, the flux values that are closest to the input model values are derived from the canonical PO model. This is true in most cases where the fitted N_H from the single PO model is significantly above the Galactic value, for both input $\Gamma = 1.7$ and 2.5. However, this canonical PO model does provide a less accurate value of the true flux compared to the DBB model when a significant disk is present. Therefore, when providing flux values for sources with parameters determined from single-component models (when N_H is enhanced), the flux from the canonical model should be used as an estimate of the true flux, except when the DBB model best-fit value of N_H is consistent with Galactic absorption, indicating that the source is in a TD state. In these instances the DBB flux value should be taken as a closer estimate of the source flux.

It should be noted that the interpretation of these spectral models has made the assumption that these sources are not embedded within diffuse emission arising from the hot gas within the galaxy. In the instances where the galaxy contains a substantial interstellar medium (ISM) care should be take to determine if the enhanced values of N_H are a consequence of intrinsic emission or caused by the surrounding medium of the source. Further, intrinsic absorption from the source itself, e.g., a warped accretion disk; as proposed for the BH–GC source in NGC 4472 by Shih et al. (2008), cannot be ruled out when enhanced values of N_H are determined in the spectra.

4.2. Cool-disk Models

In the previous section, simulations covering the range of parameters that have been observed in LMXBs in three spectral states: hard, TD, and the SPL state have been presented. In this section, the simulations are extended to include spectra that have been observed in X-ray binaries with SPL characteristics, but have cooler inner-disk temperatures than are typically observed for sources in this state ($kT_{in} < 0.4$ keV). From spectral modeling of *RXTE* observations of Galactic sources with this emission (e.g., XTE J1550−564; Kubota & Done 2004) it has been suggested that these sources appear to have a cooler disk component due to the presence of a Comptonizing corona coupling with the disk, altering the intrinsic properties of the accretion disk (Done & Kubota 2006). This type of cool-disk spectrum has also been observed in ULXs, albeit with shallower photon indices (∼1.7, e.g., Soria et al. 2007). This ULX emission has been likened to the spectra observed in Galactic binaries in outburst (Kubota & Done 2004), where the explanation

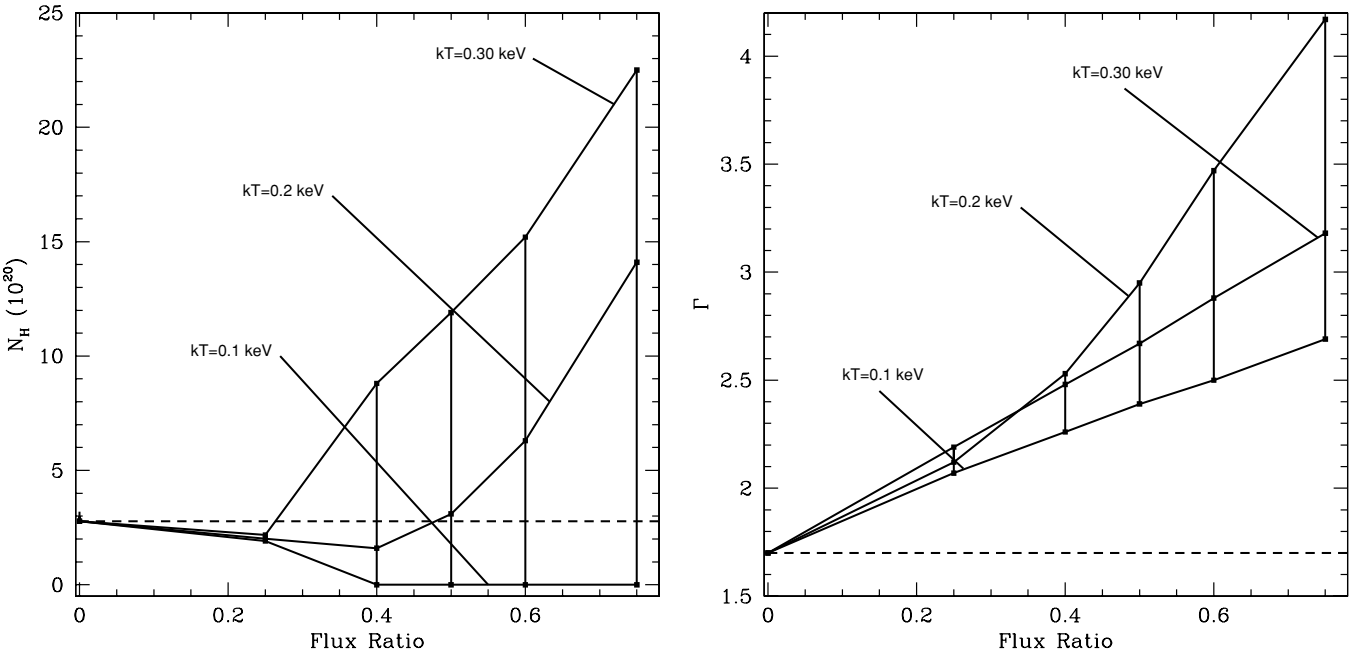

Figure 13. Best-fit results from the cool-disk simulations presented in Section 4.2, following the same presentation as Figure 9. Only the best-fit values derived from the $\Gamma = 1.7$ simulations are presented. In the right panel, the best-fit value of Γ is shown (instead of Δ photon index).

of a Comptonizing component altering the properties of the accretion disk has again been suggested.

To investigate the range of parameters obtained from single-component modeling of this cool-disk spectral state, simulations were produced with input inner-disk temperatures of 0.1, 0.2, and 0.3 keV, and photon index values of 1.7 and 2.5; representing both ULX and Galactic LMXB spectra. Flux-ratio values of 75%, 60%, 50%, 40%, 25%, and 0% were produced for each set of input parameters. A summary of the single-component PO models of these simulated spectra is presented in Figure 13, following the same convention as in Figure 9. In this figure, only the $\Gamma = 1.7$ input models are indicated in both plots for clarity. From the left-hand panel in this figure, where values of $N_{\rm H}$ are presented, it can be seen that when the source has a high flux ratio (with $kT_{\rm in} > 0.1$ keV) the best-fit value of $N_{\rm H}$ is much higher than that of Galactic, as was seen in the previous simulations. As the non-thermal component becomes more prominent the value of $N_{\rm H}$ decreases and in fact, for flux-ratio values <25%, the best-fit value of $N_{\rm H}$ is either consistent with or below Galactic for disk temperatures of 0.3 keV, and below Galactic with a flux-ratio value of <50% for $kT_{\rm in} = 0.2$ keV. For the simulations with an inner-disk temperature of 0.1 keV all values of $N_{\rm H}$ are 0, only becoming consistent with Galactic $N_{\rm H}$ with flux ratios <25%.

The best-fit values of $N_{\rm H}$ derived from the simulations with the non-thermal component described by a PO with $\Gamma = 2.5$, exhibited similar variations to those presented in Figure 13, with all $N_{\rm H}$ values from the 0.1 keV inner-disk simulations < Galactic $N_{\rm H}$. However, there were differences between the 0.2 and 0.3 keV simulations from the different Γ values, with the single-component fits from the steeper value of 2.5 always determining a best-fit $N_{\rm H}$ higher than Galactic for all flux-ratio values, apart from 0%.

The single-component DBB models for the cool-disk simulations were statistically rejected in 100% of cases when the input photon index was 1.7. When a slope of 2.5 was used, the 0.2 and 0.3 keV disk temperature simulations were adequately described by single-component models in <50% of cases. When these fits were statistically acceptable the best-fit value of $N_{\rm H}$ was 0. When the inner-disk temperature was 0.1 keV, none of the simulated spectra were statistically acceptable.

4.3. Different Absorption Models

In the simulations that have been presented in this paper the *phabs* model (Balucińska-Church & McCammon 1992) has been used to describe the absorption of X-rays in the ISM. However, other models of neutral absorption such as *wabs* (Morrison & McCammon 1983) and *tbabs* (Wilms et al. 2000) are also commonly used to describe the emission from X-ray binaries.

To determine if the results from the *phabs* simulations are consistent with results from alternative absorption models, a subset of simulations was generated using both *wabs* and *tbabs* models. To investigate the range of parameters obtained from single-component modeling of these different absorption models, simulations of a 1000 counts were produced for sources with input inner-disk temperatures of 0.50, 1.00, and 2.25 keV, and with a photon index value of 1.7. Flux-ratio values of 100%, 90%, 75%, 60%, and 40% were produced for each set of input parameters. A summary of the best-fit $N_{\rm H}$ values from the single-component PO models of these simulated spectra is presented in Figure 14, following the same convention as in the left-hand panel of Figure 9. In this figure, the diagonal black lines indicate the *phabs* model, the green lines the *tbabs* model, and the blue lines the *wabs* model. The standard deviation of each derived value of $N_{\rm H}$ is indicated by the color-coded error bar in the top left corner. From this it can be seen that all three models result in similar values of $N_{\rm H}$ and are identical within the standard deviation. The best-fit values of $N_{\rm H}$ from the single-component DBB model were also compared, and all three models again resulted in almost identical best-fit values of $N_{\rm H}$, with the fitted absorption column tending to 0 as the flux ratio decreased. These comparisons demonstrate that when spectrally modeling low-count data with single-component models, the selection of either *wabs*, *phabs*, or *tbabs* in the spectral model will result in the same behavior outlined in Section 4.1.

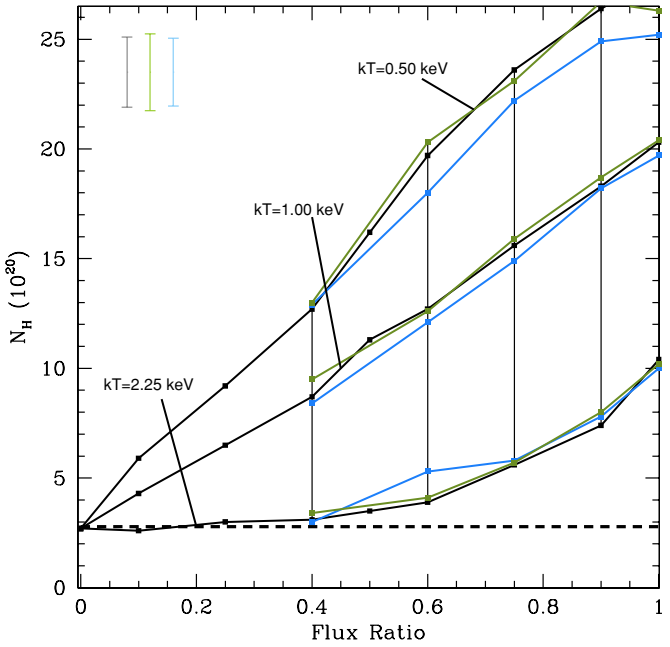

Figure 14. Best-fit results of simulations using three different photoelectric absorption models (detailed in Section 4.3) following the same presentation as in the left-hand panel in Figure 9. Here, only the best-fit values derived from the $\Gamma = 1.7$ simulations are presented for values of $kT_{\rm in} = 0.50$, 1.00, and 2.25 keV, over flux ratio values of 40%–100%. The results from the *phabs* absorption simulations are labeled by the black diagonal lines, the results from the *tbabs* simulations are shown by the green lines, and the results from the *wabs* simulations are plotted in blue. Error bars in the top left indicate the standard deviation for each set of simulations, these are also color coded. The horizontal dashed line indicates Galactic $N_{\rm H}$.

(A color version of this figure is available in the online journal.)

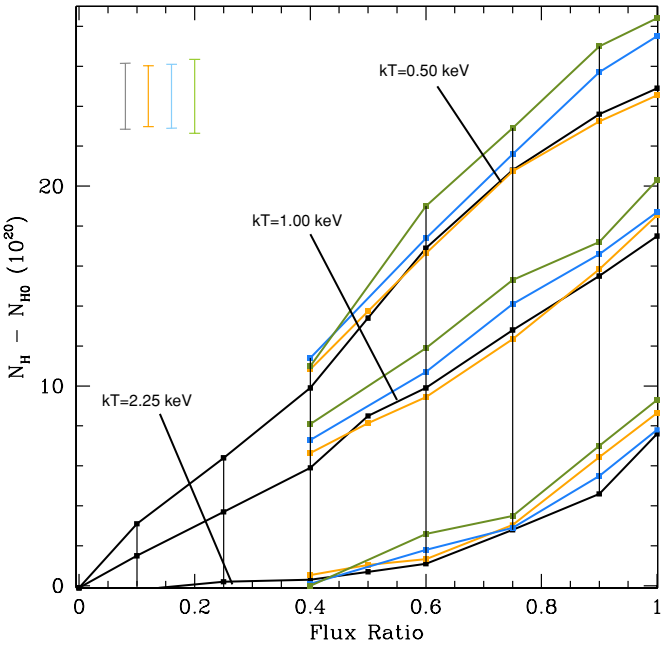

Figure 15. Best-fit results of simulations using four different Galactic absorption values (see Section 4.4 fore more details). In this figure, instead of presenting the best-fit value of $N_{\rm H}$, as shown in Figure 9, the value of excess $N_{\rm H}$ is plotted against the disk-to-total flux ratio, where the excess $N_{\rm H}$ is defined as the best-fit $N_{\rm H}$ value normalized by the Galactic absorption used in the simulations ($N_{\rm H}$–$N_{\rm H0}$). Here, only best-fit values derived from the $\Gamma = 1.7$ simulations are presented for values of $kT_{\rm in} = 0.50$, 1.00, and 2.25 keV, over flux ratio values of 40%–100%. The results from the main simulations are labeled by the black diagonal lines (with $N_{\rm H0} = 2.78 \times 10^{20}$ cm^{-2}), the results from the NGC 4278 simulations ($N_{\rm H0} = 1.76 \times 10^{20}$ cm^{-2}) are shown by the orange lines. The results from the $N_{\rm H0} = 5 \times 10^{20}$ cm^{-2} simulations are plotted in blue and the $N_{\rm H0} = 1 \times 10^{21}$ cm^{-2} simulations are indicated by the green diagonal lines. Error bars in the top left indicate the standard deviation for each set of simulations, these are also color coded.

(A color version of this figure is available in the online journal.)

4.4. Simulations Applied to Other Galaxies

To investigate how the single-component best-fit parameters altered when applying the models to galaxies with different values of absorption column, a subset of simulations was performed. For the first case, simulations were produced for NGC 4278, an elliptical galaxy with a line-of-sight absorption below that of the current simulations (1.76×10^{20} cm^{-2} compared to 2.78×10^{20} cm^{-2}).[18] These simulations were performed using response files from spectral extraction of sources within the galaxy, and input parameters were set to cover inner-disk temperatures of 0.50, 1.00, and 2.25 keV, with a fixed photon index of 1.7. Flux-ratio values from 40% to 100% were investigated, with all simulated spectra produced with 1000 counts to allow comparisons to be made with the models presented in Section 4.1. This subset of simulations was then extended to determine the best-fit parameters for systems with Galactic absorption values of 5×10^{20} cm^{-2} and 1×10^{21} cm^{-2}, with input parameters defined to cover the same Γ, $kT_{\rm in}$, and flux-ratio values as for the NGC 4278 simulations.

A comparison of the results from these four sets of simulations is presented in Figure 15, where the excess absorption column values from the single-component PO models are shown. These excess $N_{\rm H}$ values are defined as the best-fit value of $N_{\rm H}$ normalized by the simulated Galactic absorption ($N_{\rm H0}$). In this figure, the black lines indicate the simulations produced for NGC 3379, the orange lines the excess $N_{\rm H}$ values of the NGC 4278 simulations, blue the $N_{\rm H0} = 5 \times 10^{20}$ cm^{-2} simulations, and the green lines the $N_{\rm H0} = 1 \times 10^{21}$ cm^{-2} simulations. In the top left corner, color-coded error bars indicate the standard deviation of each set of simulations. What can be seen from this figure is that all simulations exhibit the same behavior of increasing values of excess $N_{\rm H}$ as the thermal component of the source becomes more prominent. In fact, all excess absorption values from the four different sets of simulations are identical within the standard deviations. The spectra from these simulations were also fitted to single-component DBB models, where the best-fit $N_{\rm H}$ values followed the behavior shown in Figure 11. This indicates that these simulations are applicable in all galaxies, where single-component best-fit values can be used to determine the presence or the absence of a thermal component, as well as the intrinsic source parameters.

[18] This galaxy is the subject of a companion paper, Fabbiano et al. (2010).

4.5. Decision Tree

Figure 16 provides a summary indicating how the best-fit parameters derived from the single-component models can be used to determine the spectral state of a source. This is presented in the form of a decision tree, indicating how best-fit values of $N_{\rm H}$ from the PO and DBB models can be used to discriminate between NT, TD, and intermediate states, including sources containing a cool-disk component.

5. DISCUSSION

From the spectral analysis of the eight sources presented in this paper, a diverse range of temporal characteristics has

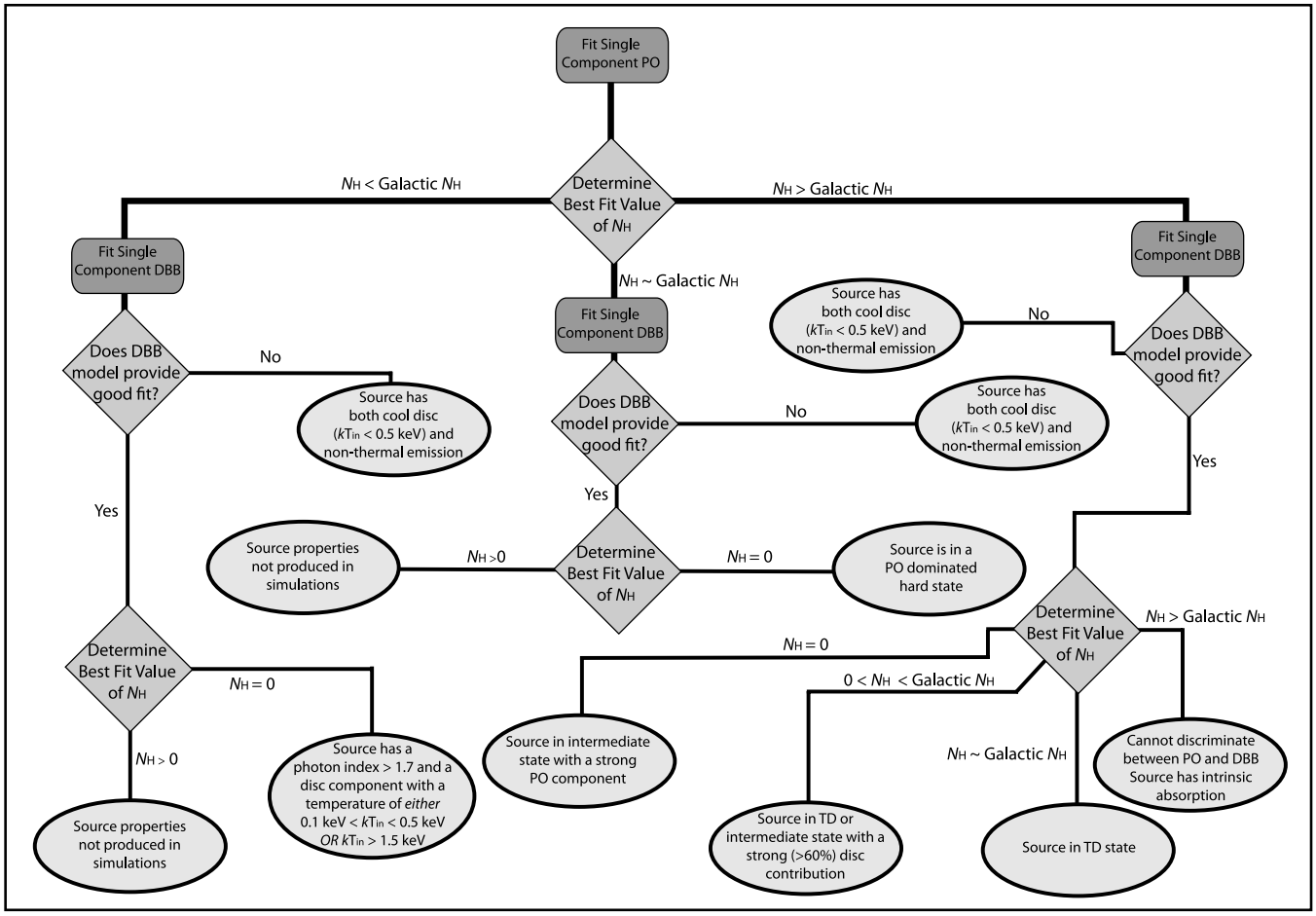

Figure 16. Decision tree summarizing how the best-fit absorption values from the PO and DBB single-component models from the simulations can be used to determine spectral source states. In this figure, the interpretation of each combination of $N_{H(PO)}$ and $N_{H(DBB)}$ is presented in the ellipses, where TD, NT, and intermediate source states are given, including sources with cool-disk components.

been identified in the bright ($L_X \geqslant 1.2 \times 10^{38}$ erg s^{-1}) LMXB population of NGC 3379. Here, the properties of the four sources determined to exhibit spectral variability are presented individually and their best-fit parameters are compared to the spectral simulations discussed in Section 4. The spectral parameters of the remaining four sources are also presented and the overall properties of this bright population are discussed.

5.1. A Black Hole GC–LMXB

Of the three GC–LMXBs that are presented in this paper, S42 is both the most luminous and the most variable. From Figure 2 it can be seen that there is a significant increase (and subsequent decrease) in flux between observations implying $\Delta L_X \sim 2.5 \times 10^{38}$ erg s^{-1} in the simple assumption of a canonical PO spectrum used to derive Figure 2 (B08). This pattern of variability is fairly common for LMXBs (van der Klis 1994). The large flux variation observed very strongly indicates that S42 is not a superposition of multiple NS–LMXBs but a single source. In fact, if it is conservatively assumed that the total luminosity is from the contribution of multiple sources, the luminosity from a single source would have a lower limit of $\sim$2.5 $\times$ 10^{38} erg s^{-1}(increasing to $\sim$7 $\times$ 10^{38} erg s^{-1} if the emission arises from a single source). This luminosity is above the Eddington limit for an NS binary (although would be close to the limit of a heavy (2–3 $M_\odot$; Kalogera & Baym 1996) NS, or a 1.4 $M_\odot$ NS with an He or C/O donor) and indicates that the source is likely to be a BH binary system.

Based on the X-ray luminosity, HR values and colors of this source, the spectra were separated into three different groups. In all three cases both single-component models provided statistically acceptable fits to the data. In the PO model, the spectral groups provided a range in Γ of $\sim$2.1–1.7, which is within the range of a hard state BH–LMXB. However, in all three cases a large intrinsic N_H, of order six times the Galactic column, was required to provide an adequate description of the data. Such large N_H columns are not usually seen in LMXBs and would be especially difficult to explain in a sub-Eddington low-state source, where outflows are not expected. One explanation could be that the lower luminosity state is a consequence of foreground absorption from a warped disk (as advocated for the variable BH–GC source in NGC 4472, which showed variability consistent with arising from changes in N_H; Shih et al. 2008). However, since there is little variability detected in N_H between spectral groups for S42, this mechanism is unlikely to be the cause of the change in L_X. Instead, from the simulations presented in Section 4, there is an indication that when a source has a significant flux contribution from a thermal disk component, the single-component PO model will provide an elevated absorption column, caused by the soft emission arising from the disk. Further, the DBB single-component modeling from the simulations indicates that when a source is in a TD state the best-fit absorption column >0, becoming consistent with

Galactic absorption as the accretion disk completely dominates the flux contribution (see Figure 11).

Indeed, the DBB best-fit models of S42 suggest that this source is predominately in a TD state over observations 1–4, where $N_{\rm H}$ ranges between (0.6–3.2) $\times$ 10^{20} cm^{-2}, possibly entering an intermediate state in observation 5, where its likely that the thermal and non-thermal fluxes contribute equally to the emission. This disk component in the TD state appears to be at its most dominant when the source is at its most luminous, in spectral grouping 2, where the best-fit value of $N_{\rm H}$ is consistent with Galactic and $kT_{\rm in} \sim 1.5$ keV, which infers a mass of $\sim 4\,M_{\odot}$ (cf. Gierliński & Done 2004). This best-fit model provides a luminosity of $\sim 9.1 \times 10^{38}$ erg s^{-1}, which further strengthens the interpretation that this source is a BH binary, where flux variability indicates that there must be a source with $L_{\rm X} > 4 \times 10^{38}$ erg s^{-1} within the GC. The increase in temperature coupled with the increase in luminosity observed between the spectral groupings could be explained as the disk's response to a temporary increase of the accretion rate, or could be due to the failure of the single-component model to adequately describe the properties of the spectra as the PO component becomes more prominent. However, the statistics in these spectra do not constrain more complex models (e.g., PO+DBB) to allow this to be investigated further.

What is very likely from these spectral properties is that a single BH binary has been detected within a GC in NGC 3379, in addition to the BH–GC within NGC 4472 (Maccarone et al. 2007) and the suggested IMBH–GC in NGC 1399 (Irwin et al. 2010). Further, it has also been determined that this source is in a TD state when it is at its most luminous. Maccarone et al. (2007) find that the BH–GC in NGC 4472 is in a very luminous ($\sim 7 \times 10^5\,L_{\odot}$) and metal-poor GC and Irwin et al. (2010) determine that the source in NGC 1399 is in a luminous ($\sim 3 \times 10^5\,L_{\odot}$) but metal-rich GC. In NGC 3379 not only S42, but also the two other GC–LMXB sources; S41 and S67, are also found in luminous GCs (B08), with luminosities of order $1.5 \times 10^5\,L_{\odot}$, $3 \times 10^5\,L_{\odot}$, and $2 \times 10^5\,L_{\odot}$, respectively, therefore following the trend identified in previous GC–LMXB studies (e.g., Kundu et al. 2007). Using the color–metallicity relations in Smits et al. (2006) and the GC colors reported in B08, we find that S41 and S67 are in "blue" low-metallicity clusters ($V - I = 0.85$ and $V - I = 0.87$; $\sim 1/10$ solar), whereas S42 is in a "red" high-metallicity cluster ($V - I = 1.12$).

These comparisons, albeit based on only five objects, are in agreement with the conclusion that GC mass may be a factor in retaining a BH–LMXB. However, given that this paper only concentrates on the brightest LMXBs within NGC 3379, we do not speculate on the suggestion that the more massive GCs host the more luminous LMXBs (Kundu et al. 2007). In fact, from B08 it has been determined that there are two less luminous LMXBs that reside in more luminous GCs than the sources presented here. Further, in the cases of S41, S67, and the source in NGC 1399, without large temporal luminosity variations it cannot be ruled out that these GCs may contain a superposition of less luminous NS rather than a single bright BH. However, due to the large variability in both S42 and the source in NGC 4472, it can be confirmed that these sources are bright single objects.

5.2. A Field BH–LMXBs

S86, the only confirmed field source with $L_{\rm X} \geqslant 10^{38}$ erg s^{-1} within NGC 3379, exhibits similar $L_{\rm X}$ variability to that of the BH–GC, S42. However, in this case, when the source is observed in its less luminous state the spectra are consistent with either a hard state, where $\Gamma \sim 1.5$ and no extra absorption is required, or possibly a cool-disk model. This latter interpretation is proposed as the best-fit value of $N_{\rm H}$ tends to 0 when left free to vary and the single-component DBB model is statistically rejected when applied to these spectra. When investigating the cool-disk simulations, such behavior was observed in both these single-component model fits (see Section 4.2). In the higher flux observations, the DBB model describes the spectra well, where the best-fit inner-disk temperature is $\sim$1.4 keV, consistent with the TD state of a $\sim 5\,M_{\odot}$ BH. The PO model also provides an acceptable description of the spectra in this higher flux state, with $\Gamma \sim 1.6$, typical of hard-state spectra. However, in this more luminous state, while the spectral index indicates an NT source, the absorption column is a factor of 4 greater than the Galactic $N_{\rm H}$. This could again point to the single-component model failing to describe the nature of the accretion, indicating a change in spectral state from the NT to the TD state (as investigated in the simulations in Section 4), or it could indicate the presence of a warped disk, as discussed in Shih et al. (2008). In both models, the source luminosity exceeds the NS Eddington luminosity, with $L_{\rm X}$ ranging between $\sim 7 \times 10^{38}$ erg s^{-1} in the NT state (or cool-disk) observations (where this high $L_{\rm X}$ also indicates that this source is not residing in the NT state) and $\sim 5 \times 10^{38}$ erg s^{-1} in the TD state spectra, which is therefore consistent with emission from a stellar-mass BH.

5.3. Spectral State Change of Central Region LMXB

S74 resides in the central region of the galaxy where the optical data become confused and therefore has an unclassified optical correlation. The spectral behavior of this source is very stable in the first four observations, where the spectra are well fitted with a $\Gamma \sim 1.6$ PO model with no intrinsic absorption, consistent with an NS or BH–LMXB in the hard state. Although, this source could have a cool-disk component, given that $N_{\rm H}$ tends to 0 when left free to vary in the PO model, and the DBB model provides a poor description of the data. In observation 5, the spectral emission changes dramatically, increasing in flux and altering in spectral state, where the PO model indicates that the source has become softer and the absorption column has increased. This is again interpreted as an indication that the disk emission has become more prominent in the source, where the DBB model describes the spectra well, although $N_{\rm H}$ left free to vary provides a best-fit value well below Galactic and has therefore been frozen in the final model. These parameters indicate that the source is in a TD state, with an inner-disk temperature of $\sim$0.7 keV and an intrinsic luminosity of $\sim 7.5 \times 10^{38}$ erg s^{-1}, that, if following the $M \propto T^{-4}$ relation, indicates that the source is a $\sim 75\,M_{\odot}$ BH. However, as the absorption column from the DBB model is below the Galactic value it is possible that a non-thermal component is present in the source, therefore this derived mass should be treated as an upper limit.

5.4. A Luminous Cool-disk Source

The final source with spectral variability is S102, which is just outside the *HST* FOV. From the plots indicating the variability in $L_{\rm X}$ and HR (Figure 2) alone it appears that this source is gradually transitioning from a bright hard source to a lower luminosity soft source. However, from the spectral groupings it has been determined that the source actually resides in distinct states. In the first observation, the spectrum is well described

by a steep power law ($\Gamma \sim 2.6$) with no intrinsic absorption. This photon index value is steeper than would be expected for a source in the hard state (RM06: $\Gamma < 2.1$), suggesting that the source is in an SPL state. However, given that the single-component DBB model is statistically rejected when fitted to this spectra, this source could be in an intermediate state with a cool-disk component (see Section 4.2). Although, within errors, both $N_{\rm H}$ and Γ are consistent with the expected values of an SPL state source, and there are too few counts in the data to allow additional components to meaningfully constrain the spectral parameters.

In observations 2 and 3, the spectra exhibit very similar properties to those observed in observation 1 although, with a greater number of counts, it is clear that the fit value of $N_{\rm H}$ from the PO model is significantly below that of Galactic absorption (see Figure 7) and consequently a two-component model has been applied to the spectra. From this best-fit model the thermal emission has been determined to have an inner-disk temperature of $kT_{\rm in} \sim 0.14$ keV, with a photon index of 1.6. A large absorption column is required for this fit, although this is not well constrained and is consistent with Galactic absorption (see contour plots in Figure 8). Such a spectrum is consistent with the properties observed in some ULXs (e.g., Soria et al. 2007) and indeed, the intrinsic luminosity of S102 in observations 2 and 3 is $\sim 1.1 \times 10^{39}$ erg s^{-1}, which does fall under the classification of a ULX, albeit at the very low end of the luminosity range. Further, the flux ratio from both of these observations indicates that 40% of the emission arises from the disk component, slightly higher than the contribution determined in Soria et al. (2007), where the thermal emission contributed 25% of the observed flux. From the $M \propto T^{-4}$ relation the temperature of this fit implies an IMBH of $\sim 5 \times 10^4\ M_{\odot}$, although, as discussed in Section 4.2, this disk may appear cooler due to the presence of a Comptonizing corona altering the properties of the disk (Done & Kubota 2006) and the true mass of the BH may be much lower.

In the final two observations of this source the luminosity decreases significantly and the flux is well described by a single-component PO model, with $N_{\rm H}$ consistent with Galactic absorption and $\Gamma \sim 1.85$, indicating that the source is likely to be emitting in an NT state. This source therefore provides observational information of a BH binary source transitioning from an SPL cool-disk state to a hard state, where the luminosity falls from $\sim 1.1 \times 10^{39}$ erg s^{-1} to $\sim 3.8 \times 10^{38}$ erg s^{-1}.

5.5. The Overall Population

In addition to the four sources that exhibit spectral variability, the four other sources included in this paper have also been analyzed. From their spectral parameters, two are consistent with being in an NT state (S41 and S77) with photon index values of $\sim$1.9 and $\sim$2.0. The two other sources (S67 and S103) have large values of intrinsic $N_{\rm H}$ from the PO model, indicating that a significant disk is present in the spectra. In the case of S67, the DBB model provides a value of $N_{\rm H}$ consistent with Galactic absorption, suggesting that the source is in a TD state, while S103 has a value tending to 0 and is therefore likely to be in an intermediate state with flux contributions from both the thermal and non-thermal components of the binary.

In Figure 17, the spectral properties of the binaries investigated in this paper are presented. In this figure, the spectral groupings of each source have either been plotted in the left or right panel, depending on their inferred state, where in the left panel log $kT_{\rm in}$ against log $L_{\rm X}$ is presented and the right panel shows Γ against log $L_{\rm X}$. When sources are likely to be in a spectral state that is not TD (or NT) the errors bars are presented as dotted lines. The best-fit values from the PO and DBB components of the luminous, cool-disk observations of S102 are indicated by the dashed error bars. In the case of the TD state for this source, this point is presented as an insert within the main plot, where a lower disk temperature range is presented. In addition to the sources, the L–T relations for a non-rotating BH (cf. Gierliński & Done 2004; Equation (3), assuming an inclination angle of 60° and $f_{\rm col} = 1.8$) of masses 5 $M_{\odot}$, 10 $M_{\odot}$, and 20 $M_{\odot}$ are indicated by the dashed lines in the left-hand plot, and an additional line indicating the L–T relation for a BH mass of 500 $M_{\odot}$ is included in the insert plot. In both panels, sources are indicated by symbol and color where labels are given in the bottom right corner.

From comparing both panels it can be seen that, in general, when a source is emitting at a lower luminosity, the spectrum indicates that the source is in an NT state, dominated by the PO component. This behavior is commonly seen in Galactic binaries, where this state was previously defined as the low–hard state, denoting both the photon index and flux of the source. However, in McClintock & Remillard (2006) it was advocated that luminosity should not be part of the classification scheme, as, while many Galactic binaries do become harder as their luminosity decreases, there are counter examples indicating that this behavior is not ubiquitous (e.g., GX 339-4; RM06). Indeed, even within the sample of sources presented here there is an indication that we observe a source transitioning between a TD and NT state while exhibiting very little change in luminosity (S86), although it is possible that these NT states (obs 1, 3, and 5) are actually in a cool-disk state. The other bright sources in the $L_{\rm X}$–Γ plot are observations 1 and observations 2 and 3 of S102. From spectral modeling it has been determined that this source is actually in an SPL or intermediate cool-disk state in observation 1 and in an intermediate cool-disk state in observations 2 and 3, both of which typically result in a higher level of flux than the NT state.

In the left-hand panel, the five sources determined to be in a TD or intermediate/TD state are presented (along with an insert presenting the TD properties of S102 in a luminous cool-disk state). The five sources within the main plot all reside in the same L–T parameter space as Galactic BH binaries (cf. Miller et al. 2004; Kajava & Poutanen 2009), albeit at the brighter end of the relation. S102, on the other hand, exhibits spectral properties that do not follow the typical relations observed in Galactic binaries (e.g., Miller et al. 2003; Stobbart et al. 2006) and could suggest the presence of an IMBH. However, as discussed in Section 5.4, with such a cool disk, while it is consistent with this interpretation, it is not proof of an IMBH.

In this figure, S42 is the only LMXB that has been determined to exhibit multiple spectral properties while in the TD state and is denoted here by the open squares. By comparing these points with the dashed lines on this plot, which indicate the $L \propto T^4$ relation; the expected signature for optically thick, geometrically thin accretion disks (Done et al. 2007), it appears that this source does not follow the standard relation, but instead roughly follows $L \propto T^{1.25}$. A flatter relation of $L \propto T^2$ has been observed in other BH binary systems at higher temperatures ($\sim$1 keV; Kubota & Makishima 2004) which has been explained as the transition of the disk from a standard accretion disk (Shakura & Sunyaev 1973) to a slim disk solution (Abramowicz et al. 1988) as the accretion rate increases. However, Gierliński & Done (2004) argue that such a transition should only occur

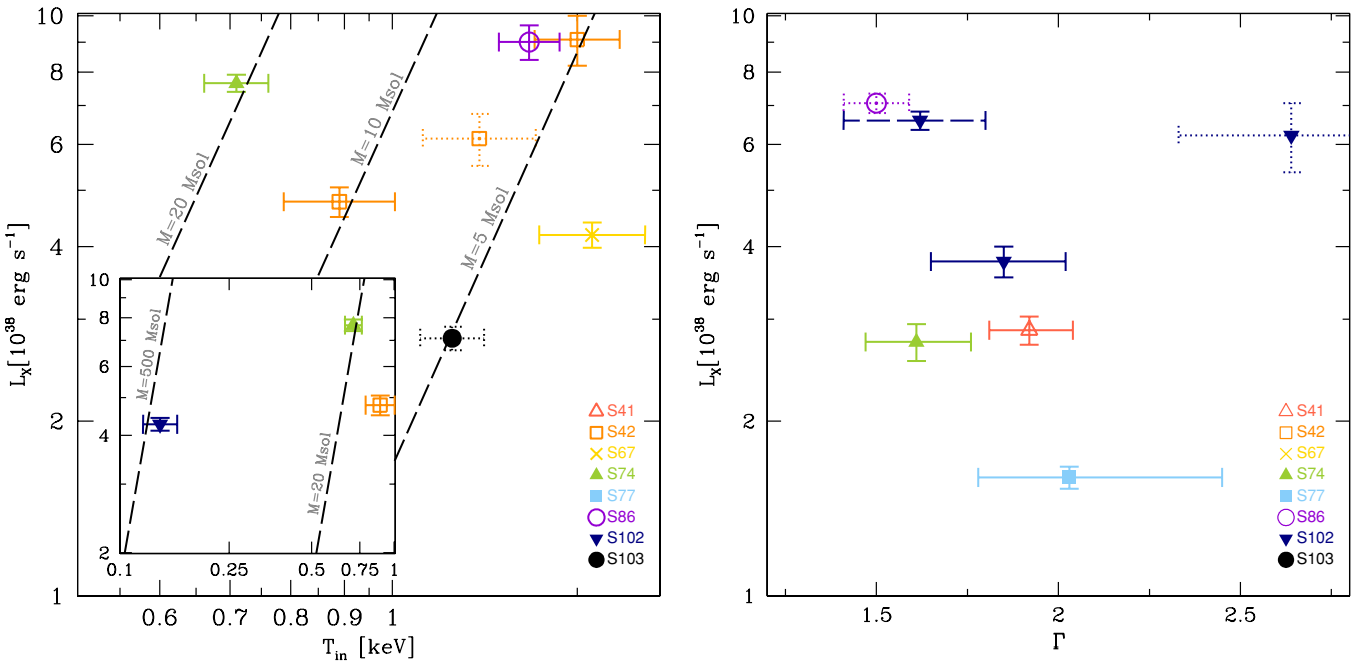

Figure 17. Population plot presenting the L_X and kT_{in} or Γ values of the eight sources presented in this paper, where multiple points are plotted for spectrally variable sources to indicate the best-fit values from each spectral grouping. In this figure, the left panel presents L_X–kT_{in} for sources in a thermally dominant state and the right panel presents L_X–Γ for sources in a hard state. In both panels, the points represent the results from the spectral fits, with 1σ errors indicated. Each source is denoted by symbol and color, with labeling provided in the bottom right corner of each panel. In cases where a source has been determined to be in an intermediate state dotted error bars are presented. In the case of observations 2 and 3 for S102, the thermal and non-thermal components are plotted separately in both panels and are indicated by dashed error bars. In the L_X–kT_{in} panel, this point is not included in the main figure but within an insert, where, due to the cool temperature of the disk (0.14 keV), the x-axis has been adjusted to cover kT_{in} values between 0.1 and 1.0 keV. In the main L–kT_{in} plot, the diagonal dashed lines indicate the $L \propto T^4$ relation for BH masses of 5, 10, and 20 $M_\odot$, following the relation of Gierliński & Done (2004). In the insert plot, in addition to these relations a line indicating $L \propto T^4$ for a BH mass of 500 $M_\odot$ is also presented.

(A color version of this figure is available in the online journal.)

above L_{Edd}, which is greater than the luminosity of sources ∼1 keV in Kubota & Makishima (2004), and they instead suggest that this flattening is associated with a change in the color temperature correction (f_{col}).

In the case of S42, the inferred mass of the BH from the M–T relation is ∼4 $M_\odot$, therefore the observed luminosity of 9.1×10^{38} erg s^{-1} would require super-Eddington accretion for a BH of this mass. This suggests that the flatter relation in Figure 17 is a consequence of the source transitioning to a slim disk, although a change in the color–temperature correction cannot be ruled out. However, this suggestion of a flatter relation should be treated with caution due to not only the limited data points, one of which is from the source in an intermediate state (observation 5) and therefore is likely to have an incorrect kT_{in}, but also due to the uncertainty in L_X from the single-component spectral modeling.

6. CONCLUSIONS

In this paper, we have investigated the spectral properties of eight bright ($L_X > 1.2\times^{38}$ erg s^{-1}) sources within NGC 3379, selected from the B08 catalog. From deep multi-pointing *Chandra* observations we have been able to determine the source properties at different epochs, and thereby characterize source spectral variability. A set of simulations used to infer the spectral states of these sources has also been presented.

Due to the luminosity cut imposed on this sample, all of the eight sources are either NS emitting at, or above the Eddington luminosity, or BH binaries, with source luminosities ranging between (1.6–10.8) × 10^{38} erg s^{-1}. From optical correlations three sources have been determined to be BH–GCs, one is detected in the field, while the remaining four sources have insufficient optical data to classify a correlation. In all cases (bar S102) single-component PO and DBB models have been applied to the data and have provided statistically acceptable fits.

To aid the interpretation of these single-component models, simulations of low-count (250, 500, and 1000) data have been presented. This work demonstrates that it is possible to determine if a source is in a hard, TD, or intermediate state by comparing the best-fit values of N_H from the two spectral models. In cases where the line-of-sight absorption in the PO fit is significantly higher than that of the Galactic value it is likely that a strong thermal component is present. If it is then determined from the DBB model, that this same source has a best-fit N_H consistent with the Galactic value it points to the source being in a TD state. If instead the DBB best-fit N_H tends to 0, it is likely that the source has both strong thermal and non-thermal components and can be said to be in an intermediate state. Although we add the caveat that while an elevated value of N_H from the single-component PO model is indicative of a TD state, intrinsic absorption arising from the disk could also explain this result in some cases. We have also provided simulations of cool-disk spectra, allowing us to identify when a source is in a high accretion state with a cool-disk component. A summary of how the best-fit values from single-component models can be interpreted is provided in Figure 16.

From these simulations it has been determined that when a source has prominent disk emission as well as a significant non-thermal component, the luminosity derived from the single-

component DBB model should be taken as a lower limit of L_X. The value inferred from the single-component PO model will be much greater than the true source value and should be disregarded. However, when a canonical PO model ($\Gamma = 1.7$ and N_H frozen to the Galactic absorption value) is applied to the data, the derived L_X value will provide the closest value to the true source luminosity. When the source is in a TD state the X-ray luminosity from the DBB should be adopted.

We have also performed these simulations for a range of different absorption values, confirming that the results are not significantly dependant on the value of Galactic absorption, demonstrating that these simulations can be used to interpret a variety of extra-galactic binary spectra. Further, different absorption models have also been used in a subset of simulations, and these results have confirmed that with low-count data the choice of absorption model does not affect the interpretation of spectral state.

Four of the eight sources presented in this paper have been determined to exhibit spectral variability and observations have been subsequently been grouped to reflect these variations. By comparing the spectral properties of these groupings to our simulations, spectral transitions have been identified. The most luminous source detected within a GC, S42, has been determined to show significant variability ($L_X > 4 \times 10^{38}$ erg s^{-1}) and can therefore be confirmed as a strong BH binary candidate, predominantly residing in the TD state. The best-fit inner-disk temperature of this source is 1.5 keV, and we estimate a BH mass of $\sim 4\,M_\odot$, providing further evidence (in addition to Maccarone et al. 2007 and Irwin et al. 2010) that GCs do retain BH binaries. If we assume that the two further GC–LMXB sources in this paper are also individual BHs, this indicates that 30% of the GC–LMXB correlations in NGC 3379 contain a BH binary, which constitutes a significant fraction of the GC–LMXB population.

A transition from a luminous SPL state to a hard state has been identified in S102 where we have identified a binary with a cool-disk component ($kT_{in} = 0.14$ keV and $\Gamma = 1.6$) emitting around the Eddington luminosity of a $10\,M_\odot$ BH ($L_X \sim 1 \times 10^{39}$ erg s^{-1}). Taken at face value, the temperature of this cool disk could suggest an IMBH. This source then declines over the 3 months between pointings to a source in a hard state, with $\Gamma \sim 1.85$ and $L_X = 3.8 \times 10^{38}$ erg s^{-1}, consistent with NT state Galactic BH binaries (RM06). The bright state of this source is similar to spectra observed in some ULXs (Soria et al. 2007) and indicates the similarities between these bright sources and more "normal" stellar-mass BH binaries in high accretion states.

The spectral properties of the eight sources are largely consistent with the parameters that have been observed in Galactic LMXBs, with sources in an NT state exhibiting a range of $\Gamma = 1.5$–1.9 and sources in a TD state with $kT_{in} = 0.7$–1.55 keV. We have also shown that this population is consistent with the general trend of increasing luminosity as sources become softer, transitioning from an NT to TD state. The L–T relation has been investigated for all the sources in a TD state, with the parameter space of these LMXBs (excepting the luminous cool-disk state of S102) being consistent with Galactic observations, albeit at the bright end of the $L \propto T^4$ relation. S42, the BH–GC, was the only source to be observed in the TD state in multiple pointings. The L–T relation of this object is flatter than the typical relation, with luminosity increasing with temperature as $\sim T^{1.25}$. Flattening has been observed in Galactic black hole binaries (Kubota & Makishima 2004) and it has been suggested that this could be due to the standard Shakura–Sunyaev accretion disk evolving into a slim disk, although this flattening could also be explained by a change in the disk color–temperature relation.

We thank the CXC DS and SDS teams for their efforts in reducing the data and developing the software used for the reduction (SDP) and analysis (CIAO). We thank the anonymous referee whose detailed and careful report has helped improve this paper. This paper is based upon work performed by S.B. while visiting CfA as part of a student program sponsored by the University of Southampton. This work was supported by *Chandra* G0 grant G06-7079A (PI:Fabbiano) and subcontract G06-7079B (PI:Kalogera). We acknowledge partial support from NASA contract NAS8-39073(CXC). A.Z. acknowledges support from NASA LTSA grant NAG5-13056.

REFERENCES

Abramowicz, M. A., Czerny, B., Lasota, J. P., & Szuszkiewicz, E. 1988, ApJ, 332, 646
Balucińska-Church, M., & McCammon, D. 1992, ApJ, 400, 699
Brassington, N. J., et al. 2008, ApJS, 179, 142 (B08)
Cash, W. 1979, ApJ, 228, 939
Done, C., Gierliński, M., & Kubota, A. 2007, A&ARv, 15, 1
Done, C., & Kubota, A. 2006, MNRAS, 371, 1216
Fabbiano, G. 2006, ARA&A, 44, 323
Fabbiano, G., et al. 2006, ApJ, 650, 879
Fabbiano, G., et al. 2010, ApJ, 725, 1824
Gierliński, M., & Done, C. 2004, MNRAS, 347, 885
Grindlay, J. E., & Hertz, P. 1985, in Cataclysmic Variables and Low-Mass X-ray Binaries, ed. D. Q. Lamb & J. Patterson (Dordrecht: Reidel), 79
Irwin, J. A., Brink, T. G., Bregman, J. N., & Roberts, T. P. 2010, ApJ, 712, L1
Ivanova, N., Chaichenets, S., Fregeau, J., Heinke, C. O., Lombardi, J. C., & Woods, T. E. 2010, ApJ, 717, 948
Jensen, J. B., Tonry, J. L., Barris, B. J., Thompson, R. I., Liu, M. C., Rieke, M. J., Ajhar, E. A., & Blakeslee, J. P. 2003, ApJ, 583, 712
Kajava, J. J. E., & Poutanen, J. 2009, MNRAS, 398, 1450
Kalogera, V., & Baym, G. 1996, ApJ, 470, L66
Kalogera, V., King, A. R., & Rasio, F. A. 2004, ApJ, 601, 171
Kim, D.-W., et al. 2009, ApJ, 703, 829
Kim, E., Kim, D.-W., Fabbiano, G., Lee, M. G., Park, H. S., Geisler, D., & Dirsch, B. 2006, ApJ, 647, 276
Kim, M., Wilkes, B. J., Kim, D.-W., Green, P. J., Barkhouse, W. A., Lee, M. G., Silverman, J. D., & Tananbaum, H. D. 2007, ApJ, 659, 29
Kubota, A., & Done, C. 2004, MNRAS, 353, 980
Kubota, A., & Makishima, K. 2004, ApJ, 601, 428
Kundu, A., Maccarone, T. J., & Zepf, S. E. 2007, ApJ, 662, 525
Maccarone, T. J., Kundu, A., Zepf, S., & Rhode, K. 2007, Nature, 445, 183
McClintock, J. E., & Remillard, R. A. 2006, in Compact Stellar X-Ray Sources, ed. W. H. G. Lewin & M. van der Klis (Cambridge: Cambridge Univ. Press), 157
Miller, J. M., Fabbiano, G., Miller, M. C., & Fabian, A. C. 2003, ApJ, 585, L37
Miller, J. M., Fabian, A. C., & Miller, M. C. 2004, ApJ, 614, L117
Morrison, R., & McCammon, D. 1983, ApJ, 270, 119
Remillard, R. A., & McClintock, J. E. 2006, ARA&A, 44, 49 (RM06)
Shakura, N. I., & Sunyaev, R. A. 1973, A&A, 24, 337
Shih, I. C., Maccarone, T., Kundu, A., & Zepf, S. 2008, MNRAS, 386, 2075
Sivakoff, G. R., et al. 2007, ApJ, 660, 1246
Smits, M., Maccarone, T., Kundu, A., & Zepf, S. 2006, A&A, 458, 477
Soria, R., Baldi, A., Risaliti, G., Fabbiano, G, King, A. R., La Parola, V., & Zezas, A. 2007, MNRAS, 379, 1313
Stobbart, A. M., Roberts, T. P., & Wilms, J. 2006, MNRAS, 368, 379
Tonry, J. L., Dressler, A., Blakeslee, J. P., Ajhar, E. A., Fletcher, A. B., Luppino, G. A., Metzger, M. R., & Moore, C. B. 2001, ApJ, 546, 681
van der Klis, M. 1994, ApJS, 92, 511
Verbunt, F., & van den Heuvel, E. P. J. 1995, in X-ray Binaries, ed. W. H. G. Lewin, J. van Paradijs, & E. P. J. van den Heuvel (Cambridge: Cambridge Univ. Press), 457
Voss, R., & Gilfanov, M. 2007, A&A, 468, 47
Weisskopf, M. C., Tananbaum, H. D., Van Speybroeck, L. P., & O'Dell, S. L. 2000, Proc. SPIE, 4012, 2
Wilms, J., Allen, A., & McCray, R. 2000, ApJ, 542, 914
Zepf, S. E., et al. 2008, ApJ, 683, L139